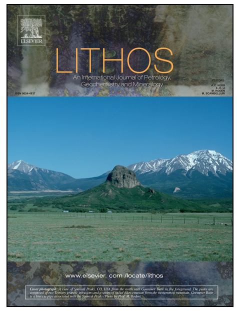

Partial melting and strain localization in metapelites at very low-pressure conditions: the northern Apennines magmatic arc on the Island of Elba, Italy

Samuele PAPESCHI, Giovanni MUSUMECI, M.A.S.S.O.N.N.E. Hans-Joachim, Omar BARTOLI, Bernardo CESARE

PII: S0024-4937(19)30389-5

DOI: https://doi.org/10.1016/j.lithos.2019.105230

Reference: LITHOS 105230

To appear in: *LITHOS*

Received Date: 28 May 2019

Revised Date: 3 October 2019

Accepted Date: 3 October 2019

Abstract

Structural and microstructural analyses and phase equilibria modeling of migmatitic amphibolite-facies metapelites from the late Carboniferous Calamita Schists, on the Island of Elba, Italy, show how the interplay between partial melting and regional (far-field) deformation assisted deformation at very shallow ($P \leq 0.2$ GPa) crustal levels. Partial melting was caused by the heat supplied by an underlying late Miocene intrusion (Porto Azzurro pluton) and occurred by biotite continuous melting. The produced melt remained in situ in patches, likely experienced limited migration in stromatic migmatites, and crystallized as a K-feldspar + plagioclase + quartz assemblage. Deformation in the presence of melt occurred by melt-enhanced grain boundary sliding, producing well-foliated high-strain zones with weak evidence of subsolidus deformation at the microscale where the original melt was present. Melt crystallization caused strain hardening and forced subsolidus deformation into localized mylonitic shear zones. The localized character of retrograde deformation was likely determined by the heterogeneous distribution/ingress of fluids in the aureole that locally assisted strain localization, enhancing dislocation creep and reaction softening.

Partial melting and strain localization in metapelites at very low-pressure conditions: the northern Apennines magmatic arc on the Island of Elba, Italy

Samuele PAPESCHI[a*], Giovanni MUSUMECI[a], Hans-Joachim MASSONNE[b,c], Omar BARTOLI[d] and Bernardo CESARE[d]

a. Dipartimento di Scienze della Terra, Pisa University, via Santa Maria 53, 56126 Pisa, Italy

b. School of Earth Sciences, China University of Geosciences, 388 Lumo Road, 430074 Wuhan, P.R. China

c. Fakultät Chemie, Universität Stuttgart, Pfaffenwaldring 55, D-70569 Stuttgart, Germany

d. Dipartimento di Geoscienze, Padova University, via Giovanni Gradenigo 6, 35131 Padova, Italy

***Corresponding author:**

Primary e-mail: s.papeschi@gmail.com

Institutional e-mail: samuele.papeschi@unifi.it

Phone: +393202472057

Address: Dipartimento di Scienze della Terra, via Santa Maria 53, 56126 Pisa (PI), Italy.

Authors' details

Samuele Papeschi; samuele.papeschi@unifi.it **ORCID** 0000-0002-5774-7119

Giovanni Musumeci; giovanni.musumeci@unipi.it **ORCID** 0000-0001-5343-4708

Hans-Joachim Massonne; h-j.massonne@mineralogie.uni-stuttgart.de **ORCID** 0000-0002-2826-4767

Omar Bartoli; omar.bartoli@unipd.it

Bernardo Cesare; bernardo.cesare@unipd.it **ORCID** 0000-0002-2340-1611

Declaration of interest:

none

Keywords: partial melting; migmatite; shear zone; strain localization; in-situ melting; pseudosections.

Highlights:

- K-feldspar + plagioclase patches record in-situ partial melting in the upper crust;
- Melting was caused by granite emplacement and occurred in the andalusite field;
- Deformation is distributed in the partially molten rocks;
- Melt crystallization causes strain localization into mylonitic shear zones;

Abstract

Structural and microstructural analyses and phase equilibria modeling of migmatitic amphibolite-facies metapelites from the late Carboniferous Calamita Schists, on the Island of Elba, Italy, show how the interplay between partial melting and regional (far-field) deformation assisted deformation at very shallow ($P \leq 0.2$ GPa) crustal levels. Partial melting was caused by the heat supplied by an underlying late Miocene intrusion (Porto Azzurro pluton) and occurred by biotite continuous melting. The produced melt remained in situ in patches, likely experienced limited migration in stromatic migmatites, and crystallized as a K-feldspar + plagioclase + quartz assemblage. Deformation in the presence of melt occurred by melt-enhanced grain boundary sliding, producing well-foliated high-strain zones with weak evidence of subsolidus deformation at the microscale where the original melt was present. Melt crystallization caused strain hardening and forced subsolidus deformation into localized mylonitic shear zones. The localized character of retrograde deformation was likely determined by the heterogeneous distribution/ingress of fluids in the aureole that locally assisted strain localization, enhancing dislocation creep and reaction softening.

1. Introduction

Partial melting is commonly regarded as an effective weakening mechanism controlling strain localization in shear zones (Hollister and Crawford, 1986; Karlstrom et al., 1993; Davidson et al., 1994; Vanderhaeghe, 2009; Kruckenberg et al., 2011). Experimental results have shown that for very low melt fraction (between 1 and 4 vol%) the dominant deformation mechanism in rocks switches from dislocation creep to melt-enhanced grain boundary sliding, in which interstitial melt allows grains to slide past each other (Cooper and Kohlstedt, 1984; Dell'Angelo et al., 1987; Dell'Angelo and Tullis, 1988; Walte et al., 2005; Zavada et al., 2007; Schulmann et al., 2008). At a higher melt fraction (~ 7-8 vol.%), melt becomes interconnected causing a further decrease in rock strength (the so called 'liquid percolation threshold' of Vigneresse and Tikoff, 1999 or the 'melt connectivity transition' of Rosenberg and Handy, 2005). Deformation in the presence of a very low melt fraction (< 7%) not only causes strain partitioning between leucosomes and the residual rocks but also activates a positive feedback mechanism attracting more melt into high-strain zones, due to the local movements of grains (Rosenberg, 2001; Walte et al., 2005; Stuart et al., 2018).

The weakening effect of partial melting and melt migration in crustal and mantle rocks has been widely investigated (Rutter and Neumann, 1995; Vigneresse et al., 1996; Vigneresse and Tikoff, 1999; Rosenberg and Handy, 2005; Misra et al., 2014), but the effect of in-situ crystallization of melt in migmatites has been broadly neglected. This is because the long-term rheology of migmatite terranes appears controlled by the efficiency of melt segregation and migration away from the residuum, causing strain hardening of the dry residual rocks (White and Powell, 2002; Brown, 2002, 2010; Guernina and Sawyer, 2003; Yakymchuck and Brown, 2014; Diener and Fagereng, 2014). However, solidification of melt has a significant impact on the rheology of melt-bearing systems, as the liquid-filled porosities are often pseudomorphed by rheologically strong phases such as feldspars. For example, in syntectonic plutons the transition from syn-magmatic shearing to subsolidus deformation is often accompanied by extreme strain localization (e.g. Gapais, 1989; Pawley and Collins, 2002; Zibra et al., 2018). A similar change in deformation style should be expected in high-strain zones in migmatites where melt crystallized in situ, for example in a melt-bearing shear zone that cooled during exhumation, or where the presence of melt was related to a transient change in thermal conditions (for example in upper crustal aureoles; e.g. Pattison and Harte, 1988; Marchildon and Brown, 2002; Johnson et al., 2003; Droop and Brodie, 2012). Stuart et al. (2018) documented the preservation of pseudomorphs after melt-filled pores in granulitic rocks that were not overprinted by subsolidus deformation due to sudden increase in rock strength caused by melt crystallization. Localization of deformation in the subsolidus regime requires the activation of softening mechanisms which may cause strain partitioning between the leucosome and the residuum and drive strain localization (e.g. Handy et al., 2001; Diener et al., 2016; Miranda and Klepeis, 2016; Stuart et al., 2018). Structures formed in the subsolidus range may be strikingly different in deformation style with respect to those formed in the presence of melt, reflecting the abrupt change in deformation mechanism and bulk rheology that follows melt solidification.

In this study, we investigated the structures recorded during transition from melt-present upper amphibolite-facies deformation to greenschist-facies mylonitization in the metasedimentary sequence of the Calamita Schists (northern Apennines, Island of Elba, Italy), within a synkinematic contact aureole developed at shallow crustal levels ($P < 0.2$ GPa). We show an example where partial melting assisted large-scale deformation in high-strain domains. At decreasing temperature, melt crystallization caused strain hardening, as melt-enhanced deformation was deactivated. The localization of deformation during retrograde deformation was locally assisted by strain softening mechanisms leading to very heterogeneous distribution of strain marked by narrow and anastomosing shear zones that overprint the high-grade foliation.

2. Geological Outline

2.1 Geology of the Island of Elba

The Island of Elba is characterized by a stack of east-verging thrust nappes that was structured between the early Miocene and the Pliocene during the development of the Northern Apennines fold-and-thrust belt (Keller and Coward, 1996; Massa et al., 2017). The nappe stack is divided into an Upper Complex, which comprises non-metamorphic to lower greenschist-facies units and a Lower Complex consisting of the medium- to high-grade metamorphic Ortano and Calamita Units (Fig. 1a). The contact between the Upper and Lower Complexes is marked by the late Miocene out-of-sequence Capo Norsi – Monte Arco Thrust (Fig. 1a) that was active up to the early Pliocene (Tab. 1; Viola et al., 2018). The nappe stack is intruded by several late Miocene intrusives, notably the Monte Capanne pluton and the Central Elba laccolith complex, emplaced in the Upper Complex, and the Porto Azzurro pluton, intruded in the Calamita Unit and buried below the present-day sea level (Fig. 1a; Barberi et al., 1967; Dini et al., 2002; Musumeci and Vaselli, 2012; Barboni et al., 2015).

The Calamita Unit was deeply affected by the late Miocene low-pressure/high-temperature (LP/HT) metamorphic imprint caused by the emplacement of the Porto Azzurro pluton, which occurred at temperatures between 600 – 650 °C and pressures below 0.2 GPa (Duranti et al., 1992; Musumeci and Vaselli, 2012; Caggianelli et al., 2018). Pluton emplacement and LP/HT metamorphism were coeval with late Miocene contractional tectonics, which determined the development of ductile syn-magmatic shear zones, which were later overprinted by brittle, post-magmatic thrust sheets at the end of the thermal pulse (e.g. Capo-Norsi Monte Arco thrust in Fig. 1a; Musumeci and Vaselli, 2012; Musumeci et al., 2015; Viola et al., 2018). LP/HT metamorphism and ductile deformation in the Calamita Unit were constrained between 6.76±0.08 Ma ($^{40}Ar/^{39}Ar$ phlogopite age) and 6.23±0.06 Ma ($^{40}Ar/^{39}Ar$ muscovite age) (Tab. 1). A zircon rim yielded a 6.40±0.15 Ma U/Pb age (see Musumeci et al., 2015). The brittle overprint was dated through ^{40}K/^{40}Ar on authigenic illite between 6.14±0.64 Ma and 4.90±0.27 Ma (Tab. 1; Viola et al., 2018). As a consequence, ductile deformation in the Calamita Unit, triggered by the thermal anomaly, very likely lasted less than 1 Ma.

2.2 Strain and metamorphic gradients in the Calamita Unit

The Calamita Unit (Fig.1a, b) is a metamorphic complex characterized by the early Carboniferous Calamita Schists, which are tectonically overlain by Triassic metaclastics (Barabarca quartzite), marbles and dolomitic marbles (Calanchiole marble; Barberi et al., 1967; Musumeci et al., 2011; Papeschi et al., 2017 and references therein). The Calamita Schists experienced LP/HT late Miocene amphibolite-facies metamorphism with peak temperatures around 625 °C (Caggianelli et al., 2018) or even exceeding 650 °C (Musumeci and Vaselli, 2012) and were overprinted by greenschist-facies retrograde metamorphism during cooling of the Porto Azzurro pluton.

The metamorphic foliation in the Calamita Schists strikes N-S to NW-SE and dips generally to the W-SW. The Ripalte antiform (Fig. 1b) refolded the main metamorphic foliation, which became E-NE dipping to (locally) subvertical in the eastern part of the Calamita Unit. The antiform is interpreted as a late thrust fault-propagation fold that affected the Calamita Unit after the LP/HT metamorphic event (see Mazzarini et al., 2011 and Papeschi et al., 2017). Stretching lineations trend E-W and dip to the W and the E on the opposite limbs of the antiform (Fig. 1b).

The Calamita Schists consists of interlayered dark grey to brownish micaschists, metapsammites, and quartzites containing centimeter- to decimeter-thick deformed quartz layers: the compositional variability is largely due to varying quartz and mica content within the schists.

Late Miocene contractional deformation is very heterogeneously distributed in the Calamita Schists, which are characterized by well-foliated high-strain domains (Fig. 2a) with local mylonitic layers and top-to-the-E kinematic indicators, localized in low-strain domains that constitute the majority of the Calamita Schists (see in detail Papeschi et al., 2017). High-strain domains display a composite fabric that preserve relic upper amphibolite-facies deformation, highlighted by grain boundary migration in quartz, overprinted by lower amphibolite- to greenschist-facies mylonitic deformation and later brittle thrusting (Papeschi et al., 2018). In the eastern part of the Calamita Unit, high-strain domains are also affected by the Ripalte antiform, becoming locally E-dipping (Fig. 1b), apparently resembling normal shear zones. Low-strain domains are characterized by poorly foliated schists and hornfelses interlayered with quartz layers, that are locally affected by E-verging tight folds (Fig. 2b).

The metamorphic LP/HT assemblage of the Calamita Schists is characterized by white mica + biotite + cordierite + andalusite, overprinted by retrograde white mica and chlorite (see in detail Papeschi et al., 2017). The highest grade rocks of the Calamita Schists are located along the southeastern coast of the Calamita peninsula, in the core of the Ripalte antiform (Fig. 1b; Mazzarini et al., 2011; Papeschi et al., 2017), where they display the typical peak assemblage biotite + K-feldspar + plagioclase + andalusite + cordierite (first recognized by Barberi et al., 1967).

3. Methodology

In the present study we describe in detail two selected areas in the highest metamorphic grade portion of the Calamita Schists, showing the peak metamorphic assemblage (biotite + K-feldspar + plagioclase + andalusite + cordierite) with evidence of partial melting and its relationship with deformational structures: Punta Bianca and Capo Calvo (Fig. 1b). Several samples, representative of the different structures and compositional domains identified in the field, were selected and analyzed in oriented thin sections (i.e. cut parallel to the lineation and perpendicular to the foliation). Details of the samples are available in the supplementary material to this article (Tab. S6) and on SESAR (https://app.geosamples.org/). Sample nomenclature strictly follows that of the SESAR database.

The petrographic microscope was used to identify mineral phases in a suite of samples, characterize microstructures, and select areas for investigations with a scanning electron microscope (SEM) and an electron microprobe (EMP). The area % of the phases present in selected samples (i.e. IESP3CS42A and IESP3SP196, see below) was estimated on thin section scans using the Color Threshold tool of the ImageJ software (Schneider et al., 2012),

Preliminary microstructural investigations and mineral analyses were carried out with a Hitachi TM3030 Plus Tabletop Microscope SEM at the Department of Earth Sciences (University of Pisa) and a ZEISS-EVO SEM equipped with an Oxford Instruments EDS detector at the National Institute for Geophysics and Volcanology (Pisa, Italy).

Rock-forming minerals were analyzed in a single sample (IESP3CS42A) with a CAMECA SX100 EMP equipped with five spectrometers and an EDS system at the Institut für Mineralogie und Kristallchemie (Universität Stuttgart). Analytical conditions for spot analyses were 15 kV accelerating voltage, 15 nA beam current, 20s counting time on peak and background each, and 1 µm spot size. Standards were wollastonite (Si, Ca), Al_2O_3 (Al), Fe_2O_3 (Fe), $MnTiO_3$ (Mn, Ti), albite (Na), orthoclase (K), olivine (Mg) and barite (Ba). Structural formulae of minerals were recalculated considering 14 oxygen equivalents for chlorite, 11 for white mica, 22 for biotite, 18 for pinitized cordierite, 8 for feldspar, 5 for andalusite, 3 for ilmenite, 5 for titanite, and 4 for rutile. Biotite was classified using the classification scheme based on the siderophyllite – eastonite – phlogopite – annite end-members after Deer et al. (1992). Concentration maps for major elements (Ca, Fe, Mn, Mg, Al and Na) were also produced by stepwise movements of the thin section under the electron beam; counting times per step were 100 ms.

The bulk rock chemistry of sample IESP3CS42A was determined by X-ray fluorescence spectroscopy (XRF) using the Panalytical PW2400 spectrometer at the Institut für Mineralogie und Kristallchemie in Stuttgart. Whole-rock analyses, expressed in wt%, were recalculated in mol% for phase equilibria modeling using THERMOCALC 3.33 (Powell and Holland, 1998; see details in section 5).

4. Structural and lithological features

4.1 Punta Bianca

The mesoscale structures exposed at Punta Bianca are developed in the biotite + K-feldspar + plagioclase + andalusite + cordierite zone of the Calamita Schists, according to Barberi et al. (1967). The foliation strikes N-S to NW-SE, gently dipping to the E (10 to 30°) and is defined by the preferred orientation of biotite, andalusite, cordierite, as well as quartz and K-feldspar + plagioclase layers (Fig. 2c, d). Upright, open to tight folds with N-S trending axes locally refold the main foliation (Fig. 2c). The Calamita Schists at Punta Bianca display a compositional banding defined by light-colored quartz-feldspar-rich layers interlayered with dark-colored biotite-rich bands (Fig. 2c, d). Moreover, millimeter to centimeter-thick quartzite layers, widely diffused in the Calamita schist from high- to low- metamorphic grade lithologies, are oriented parallel to the compositional banding. The compositional banding generally follows mesoscale structures such as folds (Fig. 2c) and foliations (Fig. 2d). Light-colored domains are composed of

K-feldspar, plagioclase, and quartz with variable content of biotite, andalusite, and cordierite, range in thickness from few millimeters to some centimeters, and are laterally continuous for several tens of centimeters (Fig. 2d, e). Dark-colored domains consist of biotite, andalusite and, less commonly, cordierite and contain discrete layers and pockets (Fig. 2f) of K-feldspar, plagioclase, and quartz. Intermediate-colored domains, characterized by a conspicuous content of both light- and dark-colored phases, are also widely present.

The foliation is heterogeneously distributed at outcrop scale and appears more penetrative in domains characterized by a higher proportion of quartz, K-feldspar, and plagioclase (e.g. Fig. 2e) with respect to dark-colored domains, that typically show randomly-distributed cm-sized andalusite grains and lack a clearly defined foliation (Fig. 2f).

4.2 Capo Calvo

Capo Calvo exposes amphibolite-facies schists and metapsammites containing biotite, quartz, andalusite, cordierite, K-feldspar, and plagioclase (Fig. 3a). The dominant fabric is a N-S to NW-SE striking and E-dipping penetrative foliation (mean dip-direction/dip: N061°/31°; Fig. 3a), defined by the preferred orientation of the amphibolite-facies assemblage, which is crosscut by anastomosing E-verging shear-zones (mean dip-direction/dip: N062°/53°; Fig. 3a) with a greenschist-facies white mica + chlorite bearing assemblage (described in detail in Papeschi et al., 2018). The eastern dip of structures at Capo Calvo is due to their position on the eastern flank of the late Ripalte antiform, which refolded originally W-dipping thrust shear zones (Fig. 1b; Mazzarini et al., 2011; Papeschi et al., 2018). Stretching lineations trend SW-NE dipping to the ENE (Fig. 3a).

As in Punta Bianca, the distribution of compositional domains and deformational features is heterogeneous at outcrop scale (Fig. 3b, c). The Calamita Schists display (1) whitish, deformed quartz-rich layers (Fig. 3b), (2) dark-colored domains (Fig. 3b, c), consisting of very poorly foliated and coarse-grained blackish nodules containing mostly biotite, cm-sized euhedral andalusite or cordierite with pockets of K-feldspar, plagioclase, and quartz, and (3) light-colored domains, consisting of foliated schists containing biotite, quartz, K-feldspar, plagioclase, cordierite, and, less commonly, andalusite (Fig. 3b). Unlike Punta Bianca, light-colored domains display a conspicuous proportion of biotite, cordierite and andalusite. As shown in Fig. 3b, the transition from light- to dark-colored domains is gradational and marked by a progressive increase in quartz-feldspathic content from the former to the latter, corresponding also to an increase in foliation intensity (see also Fig. 3c). Greenschist-facies shear zones tend to be concentrated in light-colored domains but affected also dark-colored domains (Fig. 3c).

K-feldspar and plagioclase form more-or-less elongated mm- to cm-sized patches that are heterogeneously distributed in the biotite-rich groundmass (highlighted in Fig. 3c).

5. Microstructures

5.1 Punta Bianca

Dark-colored domains

Dark-colored domains are composed of biotite, andalusite, cordierite, K-feldspar, plagioclase, quartz, and ilmenite and contain accessory tourmaline, zircon, apatite and monazite. Some domains display andalusite as part of the peak assemblage, whereas others cordierite. Very few domains contain both andalusite and cordierite. Quartz layers are locally interlayered within dark-colored domains. The foliation is generally poorly developed and the microstructure appears dominated by abundant coarse-grained (100 – 500 µm) decussate biotite grains that surround very large (> 1 mm) euhedral andalusite porphyroblasts (Fig. 4a). K-feldspar, plagioclase, and quartz are heterogeneously distributed in fine-grained polycrystalline patches with irregular shape (Fig. 4a). The intensity of foliation increases in layers characterized by a higher proportion of K-feldspar, plagioclase, and quartz (Fig. 4b). The foliation is outlined by both the preferred orientation of biotite grains and the compositional banding defined by subparallel biotite-rich and quartz-feldspar-rich bands (Fig. 4b). Well-formed and relatively coarse-grained porphyroblasts of K-feldspar and plagioclase are only sporadically present and are surrounded by a rim of interstitial K-feldspar, quartz, and rare plagioclase (Fig. S1a in supplementary material). In the vast majority of cases K-feldspar, plagioclase and quartz form polygonal, polycrystalline aggregates (grain size: 50 – 200 µm) containing iso-oriented to decussate biotite inclusions (Fig. 4c).

Biotite grains included in quartz-feldspathic aggregates frequently display a strongly irregular, resorbed outline (insert in Fig. 4c). On the other hand, biotite in large biotite aggregates (Fig. 4a) and included in K-feldspar and plagioclase porphyroblasts (Fig. S1a in supplementary material) displays subhedral to euhedral shape. Quartz, K-feldspar, and plagioclase between biotite grains frequently form a polygonal groundmass (Fig. 4d, e) that contains grains with well-defined crystal faces and triple-point junctions (as the quartz grain in Fig. 4d), coexisting with strongly irregular, interstitial grains that surround smaller grains (e.g. K-feldspar in Fig. 4e). Fig. 4f shows an example of interstitial quartz (orange) characterized by cuspate lobes interfingered between the neighboring grains, which display straight crystal faces or a rounded outline. Resorbed grains may display abundant ilmenite inclusions, which are less common in interstitial phases (Fig. 4f).

Light-colored domains

Light-colored domains consist predominantly of quartz, K-feldspar, and plagioclase with minor biotite, andalusite, and cordierite. Accessories are zircon, apatite, tourmaline, and monazite. Sericite is present as a retrograde phase, overgrowing K-feldspar and plagioclase.

As shown in Fig. 5a and 5b, the microstructure of light-colored domains is well-foliated, owing to stretched quartz grains, elongated K-feldspar + plagioclase aggregates that are often replaced by sericite, and the preferred orientation of few biotite grains. Quartz shows large grains (100 – 500 µm) that are surrounded by small (~ 10 – 50 µm) grains indicative of recrystallization by bulging and subgrain rotation (Fig. 5a). The large grains are characterized by amoeboid shape and lobate grain boundaries, indicative of grain boundary migration recrystallization (see Stipp et al., 2002).

K-feldspar and plagioclase are frequently organized in stretched layers that follow domains where few biotite grains are still preserved although strongly resorbed by cuspate lobes of K-feldspar (Fig. 5c). In spite of the strong elongation of feldspar aggregates (e.g. Fig. 5b), K-feldspar and plagioclase display a polygonal microstructure made up of polycrystalline aggregates with 50 – 200 µm average grain size that lacks extensive dynamic recrystallization features (Fig. 5d). Larger porphyroblasts (up to some hundreds of microns) are also present. In feldspar aggregates, euhedral grains of K-feldspar and plagioclase with well-developed crystal faces coexist with rounded K-feldspar, plagioclase, and quartz grains, surrounded by interstitial K-feldspar and/or quartz (Fig. 5d). Several cuspate lobes of K-feldspar with low dihedral angles penetrate between adjacent quartz and K-feldspar grains are shown in Fig. 5d as an example.

5.2 Capo Calvo

Dark-colored domains

At Capo Calvo, dark-colored domains display similar features with respect to Punta Bianca, but they are overprinted by an intense retrograde metamorphism that produced fine-grained aggregates of sericite and chlorite over biotite, andalusite, cordierite, K-feldspar, and plagioclase (Fig. 6a). Accessories are tourmaline, zircon, apatite, and monazite. Quartz is present as deformed layers with amoeboid-shaped grains.

As shown in Fig. 6a, biotite is partially replaced by andalusite, cordierite, K-feldspar, and plagioclase. K-feldspar + plagioclase + quartz aggregates with 50 – 200 µm grain size and polygonal texture occur scattered through the microstructure, surrounded by retrograde sericite (Fig. S1g in supplementary material). K-feldspar is commonly characterized by strongly cuspate and irregular lobes that penetrate between quartz and biotite grain boundaries (Fig. 6b). We observed small feldspar grains included in quartz in optical continuity with larger grains (Fig. 6b). Biotite, with strongly irregular and resorbed shape, is commonly surrounded by interstitial K-feldspar and /or quartz (Fig. 6c). The internal microstructure of K-feldspar, plagioclase, and quartz aggregates is generally characterized by a polygonal texture with euhedral grains and rounded grains that are spatially associated with interstitial K-feldspar and quartz (Fig. 6d). Interstitial grains with triangular outline, localized close to triple junctions of euhedral grains are diffuse (Fig. 6d and S1h in supplementary material).

Light-colored domains

The description of light-colored domains is focused on sample (IESP3CS42A on SESAR database) that was also investigated in detail for mineral chemistry and modeled with pseudosections (see section 7).

Sample IESP3CS42A is a schist consisting of quartz, biotite, K-feldspar, plagioclase, cordierite (pinitized), and ilmenite (in modal order; Fig. 7a), locally overprinted by retrograde sericite, chlorite, and greenish biotite. The light color of the schist is largely due to the relative high abundance of quartz and feldspars. Andalusite is very rare and was found only as a fractured porphyroclast strongly replaced by white mica (Fig. S8 in supplementary material). Accessories are apatite (grain size: 100-500 µm), tourmaline (50-100 µm), zircon, monazite (less than 50-80 µm), and titanite (50-100 µm). As shown in Fig. 7a, the sample displays a foliated microfabric defined by parallel quartz- (thickness: 1-5 mm) and biotite-rich domains (thickness: 100 µm up to 1-2 mm), together constituting 91 area% of the whole sample. The remaining 9% of the sample area is made up of K-feldspar and plagioclase (6%) and cordierite (~ 2.5%).

As shown in Fig. 7b, quartz is characterized by large grains (200 – 700 µm grain size) with amoeboid shape and strongly lobate grain boundaries, showing dissection microstructures and 'island grains' (i.e. small grains in optical continuity with larger grains; see Urai et al., 1986). Quartz grain boundaries are often pinned or dragged around subparallel biotite inclusions (pinning microstructure; see Jessell, 1987), defining the foliation within quartz-rich domains (Fig. 7c). Quartz microstructures are consistent with recrystallization by grain boundary migration (see Stipp et al., 2002). Only locally, quartz grains show patchy to undulose extinction, indicating a lower temperature overprint. Biotite-rich domains display a lepidoblastic microstructure defined by coarse-grained (100 – 500 µm) subparallel biotite grains with subhedral habit and undulose extinction (Fig. 7c) and small (~10-50 µm) subparallel grains of ilmenite. Fig. 7a highlights that cordierite, K-feldspar, and plagioclase occur strictly associated with biotite-rich layers. Cordierite forms euhedral to subhedral porphyroblasts (grain size: 0.1 –

1 mm) that are completely pseudomorphed by mixtures of phyllosilicates (i.e. pinite) still preserving equilibrium textures with the surrounding biotite-rich matrix (Fig. 7d).

K-feldspar and plagioclase occur as polycrystalline patches and augen-like aggregates that can be as large as some millimeters and are generally characterized by a grain size of ~ 100 – 500 µm (Fig. 7e). These aggregates are strictly localized in biotite-rich layers. K-feldspar is modally more abundant than plagioclase. Locally, small anhedral grains of quartz are also part of the K-feldspar + plagioclase aggregates.

As shown in Fig. 8a, K-feldspar + plagioclase aggregates are characterized by an irregular outline with several cuspate lobes protruding in the surrounding quartz and biotite (red arrows). Feldspar grains can display poikiloblastic texture due to abundant biotite inclusions. Thin (<50 µm in thickness), K-feldspar-rich layers are also localized within quartz, in correspondence of biotite-rich domains (green arrow in Fig. 8a). Biotite in contact with or included in K-feldspar shows a very irregular outline indicating replacement of biotite by K-feldspar and plagioclase (light blue arrow in Fig. 8a). A significant fraction of the smaller biotite grains included in K-feldspar and plagioclase (grain size: 5 – 100 µm) displays well-developed crystal faces, euhedral habit, and appears clearly misoriented with respect to the main foliation (insert in Fig. 8a).

The contact between K-feldspar and plagioclase aggregates and the surrounding phases is often characterized by cuspate lobes of feldspars (predominantly K-feldspar) with a smooth outline that extends for several tens of micrometers (Fig. 8b, c). Fig. 8b shows the contact of the K-feldspar rich aggregate of Fig. 8a with the surrounding quartz. Several tiny protrusions of K-feldspar into quartz and small K-feldspar grains, included in quartz, are in optical continuity with larger grains. The smaller K-feldspar aggregate of Fig. 8c, localized at the contact between biotite and quartz, displays a strongly irregular shape and is interfingered with the surrounding biotite and quartz grains. Biotite appears strongly resorbed displaying lobes of K-feldspar that penetrate biotite grains mainly along their cleavage planes (Fig. 8c). Quartz grains with either well-developed crystal faces or a rounded outline occur at the contact between K-feldspar and quartz (Fig. 8c). Lobes of K-feldspar with very low apparent dihedral angle penetrate between boundaries of quartz grains (Fig. 8c). Small films of K-feldspar (down to a thickness of 1-5 µm) diffusely occur at the contact between quartz and biotite grains or between biotite grains (Fig. 8d). The shape of K-feldspar and plagioclase grains ranges from euhedral to anhedral. As shown in Fig. 8e, many K-feldspar and plagioclase grains display sharp, planar contacts with well-developed crystal faces. Interstitial K-feldspar, plagioclase, and quartz surround euhedral to partially rounded K-feldspar and plagioclase grains (Fig. 8f).

Transition to shear zones

The transition from the light-colored/dark-colored domains to shear zones, corresponding to the transition from the foliated schists to the top-to-the-E shear zones shown in Fig. 3c, is marked by an increase in strain and a change in lithology and metamorphic grade.

An example is shown in Fig. 9a, which highlights the contact between a quartz-biotite schist (wall rock) and a cm-thick top-to-the-E shear zone (sample IESP3SP196 on SESAR and in supplementary material, analyzed via ImageJ). The wall rock consists of amphibolite-facies subparallel quartz (~60 area %) and biotite ± white mica (~25%) layers, defining a foliation obliquely oriented with respect to the shear zone boundary (dashed line in Fig. 9a), aggregates and porphyroclasts of K-feldspar and plagioclase (~13%), and cordierite porphyroclasts. White mica (incl. sericite) is present as retrograde phase locally overprinting K-feldspar, plagioclase, and cordierite. The shear zone largely (~85%) consists of very fine-grained (< 10 µm) phyllosilicates (mostly sericite) with minor very fine-grained (< 5 – 20 µm grain size) quartz ribbons (~15%) defining a penetrative mylonitic foliation (subhorizontal in Fig. 9a), locally interrupted by E-verging C'-shear bands. For a detailed description of the shear-zone microfabric, the reader is referred to Papeschi et al. (2018).

The wall rock displays a foliated microstructure characterized by subparallel quartz- and biotite-rich layers (Fig. 9b). Biotite grains (grain size: 100 – 300 µm) feature undulose extinction and numerous kink bands (Fig. 9b). Large quartz grains (up to 1 mm) with lobate boundaries and amoeboid shape, indicative of grain boundary migration recrystallization (see Stipp et al., 2002), are overprinted by undulose extinction and surrounded by small (10-15 µm) bulges with serrated grain boundaries and subgrains (e.g. Fig. 9c), which indicate low- to medium-metamorphic grade recrystallization (bulging and subgrain rotation recrystallization according to Stipp et al., 2002).

Quartz and biotite surround porphyroclastic aggregates of K-feldspar + plagioclase, compositionally dominated by K-feldspar and ranging in size from some hundreds of microns to several millimeters (as in Fig. 9d). Locally, these feldspars form layers or lenses parallel to the foliation (Fig. 9a) and display a poikiloblastic microstructure due to abundant biotite and quartz inclusions (Fig. 9d). K-feldspar and plagioclase aggregates display strain caps, where quartz and biotite are dynamically recrystallized down to 10 – 80 µm, and strain shadows containing quartz, biotite, and white mica grains or even small sericite aggregates (Fig. 9e). Bookshelf sliding of K-feldspar and plagioclase, synthetic with the sense of shear, is diffuse.

The internal structure of K-feldspar and plagioclase aggregates is characterized by euhedral to subhedral grains (grain size: 50 to 1000 µm) with well-developed crystal faces (Fig. 10a, b). Interstitial grains, usually elongated films of K-feldspar and/or quartz, are interposed between grains that in places show a linear or a rounded outline (Fig. 10a). 'String of beads' microstructures (Holness et al., 2011) locally occur associated with interstitial grains. Phase boundaries within the aggregates vary from straight to lobate or serrated (Fig. 10b).

K-feldspar and plagioclase are extensively recrystallized by subgrain rotation and bulging (grain size: 10 – 50 µm; Fig. 10c) in proximity with the shear zone boundary and occur as stretched ribbons displaying relatively large (100 - 200µm) porphyroclasts surrounded by very fine-grained grains. Quartz layers interlayered with recrystallized feldspars generally display coarser grain size (100 – 500 µm). Feldspar ribbons are in part dynamically retrogressed to white mica/sericite, forming mixed feldspar/sericite layers as in the upper right corner of Fig. 10c, or extensively replaced by sericite-dominated ribbons with a grain size of 5-20 µm, in which only few feldspar relics are recognizable (Fig. 10d).

6. Evidence of partial melting in the Calamita Schists

The Calamita Schists in Punta Bianca and Capo Calvo display the peak assemblage biotite + quartz + K-feldspar + plagioclase + ilmenite, with andalusite or cordierite (or both) depending on the protolith. Meso- and microstructural evidence (following Sawyer, 1999, 2008) suggests that the investigated rocks underwent partial melting, as we show in the following text.

We interpret the strongly replaced biotite and the K-feldspar, quartz, and plagioclase grains with rounded outline as residual phases (Fig. 4c, 6b, 8a) that were partially dissolved/consumed through melting reactions. The melt crystallized as K-feldspar + quartz + plagioclase, which are found as interstitial phases (e.g. Fig. 4f, 8d, 10a) and form cuspate lobes with a strongly irregular outline against the residual phases (e.g. Fig. 6b, 8b, 8c). In particular, interstitial films of K-feldspar with very low apparent dihedral angle (e.g. Stuart et al., 2018) that occur between biotite and quartz grains indicate crystallization within former melt-filled pores (Fig. 8d; see also

Holness and Sawyer, 2008 for similar examples). Euhedral K-feldspar and plagioclase that have crystal faces against interstitial K-feldspar, plagioclase, and quartz are interpreted as early crystallization products of melt. These feldspars may have also in part grown from residual cores (e.g. Fig. 8c, 8e). Therefore, the K-feldspar + plagioclase + quartz aggregates can be interpreted as pools and patches of former melt that contain residual grains of previously-formed metamorphic feldspars and quartz (Fig. 7e). Similar microstructural criteria to identify former melt and reactant minerals are reported by Platten (1982), Pattison and Harte (1988), Holness and Clemens (1999), Sawyer (2008), and Holness et al. (2011). We exclude that the aforementioned microstructures indicating former presence of melt might be ascribed to injection of magma, as they are invariably found throughout the investigated rocks (i.e. they do not represent a local feature) and are organized in discontinuous, diffuse interstitial films and patches rather than in discrete bodies in sharp contact with the host rocks (e.g. Fig. 2f). The occurrence of injected melts is only testified by leucocratic aplitic or pegmatitic tourmaline-bearing dykes that crosscut the metamorphic foliation/banding (e.g. Fig. 2d).

There is a strict correlation between the presence of former patches of leucosome and the availability of reactant biotite because K-feldspar + plagioclase + quartz aggregates are often found localized in biotite-rich layers (e.g. Fig. 7a), where biotite is strongly resorbed (e.g. Fig. 4c, 5c). Even in light-colored domains in Punta Bianca, where only few biotite layers are present, K-feldspar + plagioclase + quartz aggregates appear to follow reactant biotite-rich domains (e.g. Fig. 5c). These observations suggest that the elongated feldspar aggregates represent domains where all biotite reacted away, i.e. biotite layers are 'fertile' layers (Fig. 5b). Strongly resorbed biotite grains, consumed by partial melting, coexist with smaller and euhedral biotite grains that are in equilibrium with K-feldspar (e.g. Fig 8a). Such grains may be interpreted either as crystallized from the melt (i.e. liquidus phase) or as in equilibrium with the melt phase (see e.g. Platten, 1982 and Sawyer, 2008). We exclude that these grains might have been passively included, because of the strong corrosion of biotite in rocks at both investigated localities. Cordierite and andalusite, which form euhedral porphyroblasts (e.g. Fig. 4a, 8d), are interpreted to be in equilibrium with the melt-bearing peak mineral assemblage, as also suggested by the strongly resorbed shape of biotite in contact with andalusite and cordierite (e.g. Fig. 6a).

The distribution of leucosomes at the micro- and meso-scale, largely organized in discrete patches (e.g. Fig. 5c) and interstitial films or pools, led us to classify the studied rocks as patch migmatites (according to Sawyer, 2008). Only in Punta Bianca, melt appears to have been organized in discrete layers (e.g. Fig. 2e) because we interpret the compositional layering between light-colored and dark-colored domains at this locality to be the result of the original abundance of melt in the different domains. In particular, the high K-feldspar + plagioclase content of light-colored domains together with their relative low content of biotite suggests that they were originally rich in melt as a result either of fertility or melt migration. Therefore, the banded rocks of Punta Bianca can be interpreted as stromatic migmatites (according to Sawyer, 2008).

7. Metamorphic Petrology

Whole-rock and mineral chemistry was carried out on sample IESP3CS42A (Fig. 7, 8). This patch migmatite sample was chosen based on (1) the clear relationships between partial melting microstructures and the peak mineral assemblage (quartz + biotite + cordierite + K-feldspar + plagioclase) and (2) the lack of structures indicating migration and partitioning of melt into discrete leucosomes. Thus, no significant melt loss after partial melting was inferred for sample IESP3CS42A.

7.1 Mineral Chemistry

Representative mineral analyses of sample IESP3CS42A are listed in Tab. 2. All analyses are provided in the supplementary material. K-feldspar displays a Na-poor composition (Or_{90-100}) whereas plagioclase shows an oligoclase composition (An_{10-17}). Ilmenite is characterized by Mn contents between 0.05 and 0.12 per formula unit (p.f.u.) and Fe^{3+} contents < 0.01 p.f.u (Tab. 2). Concentration maps were acquired on biotite grains (1) aligned along the foliation and containing interstitial K-feldspar (Fig. 11a) and (2) included in K-feldspar (Fig. 11b). Biotite grains show in general a homogeneous distribution of Fe, Mg, and Al (Fig. 11c, d, f, g) and a zoning characterized by an increase in Ti towards the rims (Fig. 11e, h). The compositional maps of Fig. 11c, d highlight the presence of thin laminae of K-feldspar, frequently altered to sericite, localized between biotite grains. Small rutile and chlorite grains occur as alteration phases (Fig. 11d, e).

Resorbed biotite grains included in K-feldspar are characterized by lobes of K-feldspar that clearly interrupt the Ti-zoning pattern (Fig. 11h). As shown in Fig. 11f, g euhedral biotite grains included in K-feldspar are, on the other hand, compositionally homogeneous and lack any Ti-zoning pattern (Fig. 11h). Mineral analyses of biotite where distinguished based on their habit (resorbed vs euhedral). The X_{Fe} (=Fe/[Fe + Mg]) values of biotite range between 0.6 and 0.7, with euhedral biotite characterized by slightly lower Al contents and X_{Fe} between 0.60 and 0.65 (Fig. 12a). The Ti contents of euhedral biotite grains are between 0.2 and 0.3 p.f.u., comparable to that of the cores of resorbed biotite grains. Higher Ti contents, between 0.3 and 0.5 p.f.u., were detected on the rim of resorbed biotite grains (Fig. 12b, Tab. 2). We noted an increased scatter towards lower X_{Fe} values in resorbed biotite rims that we interpret as alteration along grain boundaries (Fig. 12a, b). The investigated sample contains also greenish, retrograde biotite (Fig. S10 in supplementary material), which is characterized by low X_{Fe} values and Al contents and Ti contents between 0.10 and 0.15 p.f.u. (Fig. 12a, b). Pinitized cordierite displays a large variability in Mg, Fe, and Al contents, yet showing relatively constant X_{Fe} between 0.48 and 0.58.

7.2 Geothermometry

Ti-in-biotite geothermometry was performed on sample IESP3CS42A applying the geothermometer calibrated by Wu and Chen (2015). This geothermometer was calibrated for the pressure-temperature (P-T) range of 450 – 840 °C and 0.1 – 1.9 GPa and, contrarily to the biotite geothermometer of Henry et al. (2005), is optimized for ilmenite- and/or rutile-bearing samples, making it suitable for the selected sample. Nevertheless, the geothermometer by Henry et al. (2005) was also applied to confront the results: temperature estimates resulting from the application of both geothermometers are available in the supplementary material.

For the calculation, all iron was considered to be divalent, based on the lack of Fe^{3+} bearing phases such as magnetite. The input pressure was set to 0.2 GPa (maximum metamorphic pressure for the Calamita Schists according to Musumeci and Vaselli, 2012). Temperature estimates on resorbed biotite grains range between 570 and 730 °C (average: 629 ± 57 °C; Fig. 12c) in biotite cores and 600 and 730 °C (average: 654 ± 36 °C; Fig. 12c) in biotite rims, based on the geothermometer by Wu and Chen (2015). The application of the geothermometer by

Henry et al. (2005) yielded similar results yet providing systematically ~10 – 30 °C higher temperatures compared to those obtained with the geothermometer by Wu and Chen (2015).

7.3 Phase equilibria modeling

The bulk composition of sample IESP3CS42A, expressed in wt% is: 72.52 SiO_2, 0.67 TiO_2, 14.44 Al_2O_3, 4.07 Fe_2O_3, 0.05 MnO, 1.51 MgO, 0.50 CaO, 1.53 Na_2O, 3.47 K_2O, and 0.15 P_2O_5. The bulk composition was recalculated as mol% to fit into the MnO – Na_2O – CaO – K_2O – FeO – MgO – Al_2O_3 – SiO_2 – H_2O – TiO_2 – O_2 (MnNCKFMASHTO) system, used for phase equilibria modeling (Fig. 13). For this purpose, P_2O_5 was fractionated as apatite, together with the corresponding amount of CaO. All Fe was considered as divalent, owing to the lack of Fe^{3+}-rich oxides and the negligible amount of Fe^{3+} in the analyzed minerals. However, it was necessary to use the MnNCKFMASHTO system to model ilmenite as a Fe^{3+}-free phase in THERMOCALC. Pseudosections were calculated using THERMOCALC 3.33 (Powell and Holland, 1988) and the internally consistent thermodynamic dataset ds55 by Holland and Powell (1998; updated November 2003). The following solid solution models were used: amphibole (Diener et al., 2007), silicate melt (White et al., 2007), cordierite, staurolite, chlorite (combination of Mahar et al., 1997 and Holland and Powell, 1998), garnet, biotite, ilmenite, (White et al., 2005), orthopyroxene (White et al., 2002), chloritoid (combination of Mahar et al., 1997 and White et al., 2000), muscovite, paragonite (Coggon and Holland, 2002), plagioclase, and K-feldspar (Holland and Powell, 2003). The fluid was considered to be pure H_2O (X_{H2O} = 1). The pseudosection shown in Fig. 13 was calculated assuming water-saturated conditions, as it commonly occurs in prograde metapelites in contact aureoles (e.g. Buick et al., 2004). The suprasolidus part of the pseudosection was calculated using a fixed H_2O content of 1.66 mol%, calculated using the rbi script of THERMOCALC assuming 0.5 vol.% of water at the solidus at 0.2 GPa.

Sample IESP3CS42A shows a muscovite-free assemblage, consisting of quartz + biotite + K-feldspar + plagioclase + cordierite indicating equilibration at temperatures above the muscovite-out reaction. The observed assemblage (biotite, in particular) is partially resorbed by aggregates of K-feldspar + plagioclase + quartz, which are interpreted as products of crystallization of melts, and that contain euhedral biotite grains, which were likely in equilibrium with the melt phase (see Fig. 7, 8 and par 5.2).

Phase equilibria modeling shows that the assemblage cordierite + biotite + K-feldspar + plagioclase + ilmenite + quartz is stable in an esavariant field in the subsolidus between 0.05 - 0.32 GPa and 530 – 710 °C (Fig. 13). The calculated X_{Fe} isopleths for cordierite and biotite match the X_{Fe} observed on resorbed biotite (Fig. 12b) and, in part, pinitized cordierite. The composition of biotite within the cordierite + biotite + K-feldspar + plagioclase + ilmenite + quartz field becomes progressively poorer in iron towards higher temperatures, starting from X_{Fe} ~ 0.72 at ~ 550 °C to X_{Fe} ~ 0.66 at ~ 650 °C (Fig. 13). The same trend is observed in resorbed biotite grains which show a decrease in X_{Fe} from core to rim (Fig. 12b), corresponding to a temperature range from 570 to 730 °C, based on Ti-in-biotite geothermometry (Fig. 12c). The biotite model of White et al. (2005), used for phase equilibria modeling, estimates a Ti-content of biotite for the 570 – 730 °C temperature interval, which is significantly smaller (~0.01 to 0.1 p.f.u. on a 22 oxygen basis).

The wet solidus intersects the cordierite + biotite + K-feldspar + plagioclase + ilmenite + quartz field between 0.12 and 0.31 GPa at T between 656 and 713 °C (Fig. 13). At P < 0.12 GPa, partial melting occurs in the presence of orthopyroxene and, at P > 0.31 GPa, in the presence of sillimanite (Fig. 13). The composition of biotite that is stable in the presence of melt (cordierite + biotite + melt + plagioclase + ilmenite + quartz field) is characterized by X_{Fe} < 0.66 down to 0.62 (Fig. 13) matching the observed X_{Fe} of euhedral biotite (X_{Fe} = 0.60 – 0.65; Fig. 12a, b).

8. Discussion

8.1 P-T conditions of partial melting in the Calamita Schists

This study provides field and microstructural evidence (see sect. 5) of late Miocene partial melting in metapsammites from the high-strain domains of the Calamita Schists, in the southeast of the Island of Elba. We have demonstrated the presence of both stromatic migmatites (Punta Bianca), in which melt was concentrated in bands, and patch migmatites (Capo Calvo), in which leucosomes remained unsegregated. These anatectic rocks, formed in association with shallow intrusives in the Northern Tyrrhenian magmatic arc, are the unique example of crustal anatexis in the Northern Apennines. Phase equilibria modeling (Fig. 13) constrains in-situ partial melting in the patch migmatite sample (IESP3CS42A) between 0.12 and 0.31 GPa for temperatures between 660 and 710 °C. Furthermore, Ti-in-biotite geothermometry provides an independent constraint indicating a prograde evolution with peak metamorphic temperatures reached between 660 and 730 °C. Interestingly, our Ti-in-biotite estimates overlap with the 600 – 700 °C estimates obtained by Caggianelli et al. (2018) on samples distributed on the whole Calamita peninsula, although these authors discarded these estimates, based on the interpretation that retrograde muscovite was in equilibrium with the peak mineral assemblage. Though andalusite was not present in the sample investigated for phase equilibria modeling, it occurs in the rocks nearby. The equilibrium textures of andalusite in the presence of melt (e.g. Fig. 3a), observed both in Punta Bianca and Capo Calvo, are indicative of very low-pressures of partial melting, in a fairly restricted P-T field between 0.1 and 0.25 GPa (Cesare et al., 2003). Therefore, the maximum pressure for partial melting can be set at 0.2 – 0.25 GPa. Pressures < 0.2 GPa have already been proposed for the metamorphism of these rocks (Duranti et al., 1992; Musumeci and Vaselli, 2012; Caggianelli et al., 2018), although anatexis was not considered. Moreover, the coexistence of melt and andalusite is an indication of fluid-present melting, because the dry granitic solidus do not intersect the andalusite stability field (see Le Breton and Thompson, 1988 and Cesare et al., 2003). Continuous melting in the presence of biotite without generating orthopyroxene as a peritectic phase indicates that partial melting occurred well below the biotite dehydration melting reaction (Le Breton and Thompson, 1988; Vielzeuf and Holloway, 1988), consuming the water available in the sample at and below the 'wet' granite solidus (e.g. Brown, 2002; White and Powell, 2002; Guernina and Sawyer, 2003; Vernon and Clarke, 2008). Retention of water is expected during rapid heating of low-grade metapelites in contact aureoles, in contrast to regional metamorphism which renders metapelitic rocks more dehydrated (Buick et al., 2004).

Phase equilibria modeling suggests melt productivity in the investigated sample (IESP3CS42A) between 1 and 4% in the cordierite + biotite + K-feldspar + plagioclase + ilmenite + melt field, assuming a water-saturated solidus (Fig. 13). An independent estimate, based on image analysis of the investigated sample, places the maximum amount of melt that was present at ~ 6% (area occupied by K-feldspar and plagioclase aggregates; Fig. 7a). This, however, represents an excess estimate, since feldspar aggregates preserve microstructural evidence of the presence of residual grains. Therefore, it is largely unlikely that they were completely molten.

8.2 Deformation in the presence of melt: effect on structures and microstructures

The Calamita Schists are characterized by a heterogeneous pattern of deformation which has been detailed by Papeschi et al. (2017, 2018). However, the processes that allowed shear-zone initiation in the Calamita Unit remained unclear, in particular regarding the transition from a relatively distributed upper amphibolite-facies deformation with respect to narrow and localized greenschist-facies shear zones (Papeschi et al., 2017, 2018).

In the investigated Capo Calvo and Punta Bianca sections, the mesoscale foliation is more penetrative and the average grain size is finer in light-colored domains, in which significant amounts of K-feldspar, plagioclase and quartz are present (Fig. 2d, 2e, 3b). Quartz shows deformational features like lobate grain boundaries, amoeboid shape, pinning microstructures, and island grains (e.g. Fig. 7b, c) that suggest deformation by grain boundary migration recrystallization, typical of rocks deformed at conditions of high metamorphic grade (e.g. Stipp et al., 2002; documented in detail for the Calamita Schists by Papeschi et al., 2017). On the other hand, K-feldspar + plagioclase + quartz aggregates very rarely show recrystallized grains and/or undulose extinction. In fact, they are dominated by euhedral and polygonal grains with triple junctions and straight grain boundaries, relatively uniform grain size of 100 – 400 μm, spatially associated with interstitial grains (Fig. 5d among others), suggesting crystallization from melt (see sect. 6). The undeformed appearance of K-feldspar + plagioclase + quartz aggregates, largely displaying an igneous texture that did not experience significant subsolidus recrystallization, is in striking contrast with (1) the well foliated structure of light-colored domains at the mesoscale (Fig. 2e), (2) the extensive dynamic recrystallization of the associated quartz (Fig. 5a), and (3) the strong elongation of feldspar aggregates (Fig. 5b). A key observation is that ephemeral structures, which are easily erased by dynamic recrystallization, such as (1) interstitial phases, (2) pseudomorphs after films of former melt with very-low apparent dihedral angle and (3) lobes of K-feldspar and quartz are well preserved and appear largely unaffected by dynamic recrystallization and/or annealing in high-strain zones. Furthermore, there are neither strain caps nor strain shadows surrounding feldspar aggregates, suggesting that melt-related structures were preserved at the grain scale and not obliterated by subsequent subsolidus deformation (i.e. they represented low-strain domains during development of amphibolite- to greenschist-facies shear zones). Similar microstructures, reported from granulite-facies high-strain zones, have been interpreted by Stuart et al. (2018) as evidence of deformation in the presence of melt, which can be achieved by grain boundary sliding, accommodated by the movement of interstitial melt along grain boundaries and porosity (Rosenberg and Handy, 2000; Rosenberg, 2001; Walte et al., 2005). Intergranular films of melt are indeed very common in the investigated high-strain rocks (e.g. Fig. 8d) and likely assisted the relative sliding of solid grains past each other during deformation. Deformation dominated by melt-assisted grain boundary sliding, rather than dislocation creep, is supported by the general lack of crystallographic preferred orientation in K-feldspar + quartz + plagioclase aggregates (e.g. Zavada et al., 2007; Viegas et al., 2016). Furthermore, during melt-accommodated grain boundary sliding, the solid grains did not experience solid-state deformation or migration of grain boundaries (Stuart et al., 2018). According to Dell'Angelo et al. (1987), Dell'Angelo and Tullis (1988), and Walte et al. (2005), at low melt fractions (likely between 1 and 4%) melt-assisted grain boundary sliding becomes ineffective and deformation switches to dislocation creep. The general lack of a subsolidus overprint on igneous features in feldspar aggregates and, in particular, the preservation of pseudomorphs after melt-filled pores indicates that the deactivation of melt-assisted grain boundary sliding determined a halt or decrease of deformation intensity following melt crystallization.

8.3 Strain localization during and after partial melting

The coexistence of localized igneous features with dynamic recrystallization in high-strain domains suggests that partial melting and deformation occurred together at peak metamorphic conditions in the Calamita Schists. The development of the foliation, which is more pervasive in light-colored and originally melt-rich domains with respect to dark-colored and originally melt-poor domains, clearly indicates a correlation between melt availability and intensity of deformation.

As quoted above, the presence of melt is an efficient softening mechanism even at very low melt fraction (e.g. Holyoke and Tullis, 2006; Zavada et al., 2007). On the other hand, crystallization of melt causes the deactivation of grain boundary sliding, leading to strain hardening of the system (Handy et al., 2001; Diener & Fagereng, 2014). Therefore, while the presence of melt allows strain to be pervasively distributed, the switch to subsolidus deformation necessarily causes deformation to become more localized. Strain localization in narrow high-strain zones at subsolidus conditions allows the extensive preservation of fragile melt pseudomorphs formed close to peak metamorphic conditions.

The Calamita Schists record the transition from relatively distributed upper amphibolite-facies deformation in the presence of melt, preserved both at Capo Calvo and Punta Bianca, to localized, mylonitic deformation, well documented at Capo Calvo, and even brittle shear zones (see e.g. Papeschi et al., 2018). The Porto Azzurro pluton intruded the Calamita Schists at shallow depth ($P < 0.2$ GPa; Duranti et al., 1992; Musumeci and Vaselli, 2012; Papeschi et al., 2017; Caggianelli et al., 2018). Therefore, the evolution from peak metamorphic to subgreenschist-facies conditions was likely the result of cooling to ambient temperatures around

~ 200-250 °C rather than exhumation. As shown by Papeschi et al. (2018), even assuming 1-2 mm/years of exhumation in 800 Ka, the resulting effect on pressure decrease (or increase, in case of thickening) would be minimal. In the nearby Monte Capanne intrusion, fission track ages on apatite indicate a very rapid uplift at 2-3 Ma around 1.25 mm/year of Western Elba (Bouillin et al., 1994). Considering the structural and lithological continuity of Eastern and Western Elba, the exhumation/uplift of the Calamita Unit was likely younger than the late Miocene syn-metamorphic deformation event recorded by the Calamita Schists.

Although the evolution from upper amphibolite- to subgreenschist-facies deformation was very fast (< 1 Ma; Musumeci et al., 2015; Papeschi et al., 2018) and greenschist-facies mylonitic shear zones pervasively overprinted previous structures (e.g. Papeschi and Musumeci, 2019), evidence of earlier deformation in the presence of melt is locally preserved in the shear zone walls (Fig. 9). Structures indicating former presence of melt, like interstitial grains (Fig. 10a), occur in aggregates wrapped by the metamorphic foliation and surrounded by strain caps. Quartz layers and K-feldspar + quartz + plagioclase aggregates are strongly affected by sub-solidus deformation, marked by (1) undulose extinction (Fig. 9b), (2) extensive recrystallization of quartz and feldspar to mylonitic ribbons (Fig. 10c), and (3) development of a bimodal grain-size distribution due to coexisting relic and recrystallized grains (Fig. 9c, 10c). Dynamic recrystallization of subparallel quartz and feldspathic layers is indicative of medium- to high-metamorphic grade deformation (see e.g. Vernon and Flood, 1987; Tullis et al., 2000; Hippertt et al., 2001). K-feldspar and plagioclase in particular are affected by extensive retrograde and synkinematic overgrowth of phyllosilicates that reflect the activity of reaction softening mechanisms (Mitra, 1978; White et al., 1980; Hippertt and Hongn, 1998; Mariani et al., 2006), which are commonly documented in mylonitic quartz-feldspathic rocks (e.g. Stünitz and Tullis, 2001). The retrograde growth of hydrous phyllosilicates demonstrates that water was available during deformation. The presence of fluids during deformation in high-strain zones of the Calamita Schists is also supported by a recent Electron Back Scatter Diffraction-based study that provided evidence of dissolution-precipitation creep in quartz during the development of mylonites (Papeschi and Musumeci, 2019).

Hydrous fluids might have acted as an efficient weakening component for the development of retrograde shear zones. Indeed, dynamic recrystallization of quartz and feldspar is favored under ‘wet’ conditions (hydrolytic weakening; Luan and Paterson, 1992; Post and Tullis, 1998; see also Vernon and Clarke, 2008). Localization of strain in the subsolidus region might hence be favored by the addition of external water. Circulation of fluids originated from the underlying plutonic system is well documented for the Calamita Schists (Dini et al., 2008). Moreover, the fluid released after crystallization of the melt might have infiltrated the Calamita Schists in a heterogeneous fashion, favoring strain partitioning in the fluid-rich portions of the aureole. Considering the investigated sections, we suggest that Punta Bianca was characterized by limited ingress of fluids after melt crystallization, whereas Capo Calvo was affected by fluid ingress assisting strain localization during retrograde shearing. The latter scenario is supported by the strong sericitization of the peak metamorphic assemblage at Capo Calvo.

9. Conclusions

This study provides the first evidence of late Miocene migmatite formation in a very shallow aureole in the Northern Apennines and shows an example of retrograde strain partitioning and localization in patch migmatites in an upper crustal setting. The key results of this work can be summarized as follows:

(1) Phase equilibria modeling and Ti-in-biotite thermometry constrain partial melting via continuous biotite melting between 0.1 – 0.25 GPa and 660 – 710 °C in the andalusite field.

(2) Deformation concentrated in light-colored domains that represent leucosomes. Metamorphic quartz only displays extensive evidence of recrystallization by grain boundary migration and K-feldspar + quartz + plagioclase pseudomorphs after melt, which filled porosities, lack significant evidence of subsolidus deformation. Therefore, we suggest that deformation was assisted by melt-enhanced grain boundary sliding and ceased after crystallization of the melt.

(3) Melt crystallization determines strain hardening of the rocks, forcing a change in deformation style from distributed to localized in high-strain mylonitic shear zones. Mylonites preserve the transition from amphibolite-facies deformation in the presence of melt to dynamic recrystallization with the development of mylonitic ribbons. Heterogeneous fluid ingress is envisaged as being responsible for localized strain softening in high-strain zones during retrograde conditions.

Acknowledgements

This manuscript greatly benefited from the excellent reviews by Johann Diener and an anonymous reviewer. We thank Marco Scambelluri for editorial handling. We are grateful to Thomas Theye and Federico Lucci for many fruitful discussions and guidance with the microprobe in Stuttgart. Paolo Garofalo and Luca Pandolfi are warmly thanked for granting access to their personal microscopy facilities. Omar Gianola is also thanked for assistance with the microscopy equipment in Padova. We thank the Tenuta delle Ripalte estate for providing access to their property on the Calamita peninsula.

Funding: this work was supported by the University of Pisa (PRA_2016, Resp. Sergio Rocchi), by the PEGASO PhD program (Tuscany Region, Italy) and by the Erasmus+ exchange program of the European Union.

Data Availability

The microprobe source files (settings, core files and exported images), XRF analysis and phase equilibria modeling files related to this manuscript are available at Papeschi, Samuele; Musumeci, Giovanni; Massonne, Hans-Joachim (2019), "Microprobe and pseudosection data - Sample IESP3CS42A - Calamita Schists - Elba (Italy)", Mendeley Data, V2 http://dx.doi.org/10.17632/c6ghw55sg4.2

Figure Captions

Figure 1 – (a) Simplified structural-geological map of Island of Elba (modified after Papeschi et al., 2017). The rectangle marks the insert of Fig. 1b. (b) Geological sketch map of the eastern coast of the Calamita peninsula, showing the position of the study areas, also with respect to the Ripalte antiform. Mineral abbreviations: And: andalusite; Bi: biotite; Cd: cordierite; Di: diopside; Ksp: K-feldspar; Phl: phlogopite; Pl: plagioclase; Tr: tremolite; Wm: white mica; Wo: wollastonite.

Figure 2 – (a-b) Mesoscale features of the Calamita Schists in the Wm + Bi + Cd + And zone. (a) Foliated micaschists with deformed quartz layers. **(b)** Folded quartz layers surrounded by biotite-rich schists. The yellow dashed line highlights the fold pattern. **(c-d-e-f)** The Calamita Schists at Punta Bianca (location in Fig. 1b), showing subparallel quartz layers, light-colored quartz-feldspar-rich domains and dark-colored And/Cd + Bi domains that follow **(c)** folds and **(d)** the main mesoscopic foliation. **(e)** Detail of the relationships between dark-colored and light-colored domains, highlighting the increase in foliation intensity in light-colored domains. **(f)** Andalusite-rich unfoliated dark-colored domain containing irregular Ksp + Pl + Q pockets. Mineral abbreviations: And: andalusite; Bi: biotite; Cd: cordierite; Ksp: K-feldspar; Pl: plagioclase; Q: quartz; Tur: tourmaline; Wm: white mica.

Figure 3 - (a) Sketch geological map of Capo Calvo with sample and figure locations. Poles to the foliation and shear zones and stretching lineations are shown in the insert stereographic projection (equal angle, lower hemisphere). The ellipse marks the trace of the 95% confidence cone of the mean lineation vector (yellow star). **(b-c)** Mesoscale features at Capo Calvo: **(b)** Transition from dark-colored, weakly foliated domains to light-colored, well-foliated domains. Note the presence of deformed quartz layers. **(c)** Detail of light-colored domains showing well-developed amphibolite-facies foliation crosscut by E-verging shear zones. The red arrows highlight patches of K-feldspar + plagioclase + quartz. And: andalusite. Bi: biotite. Cd: cordierite. Ksp: K-feldspar. Pl: plagioclase. Q: quartz.

Figure 4 – Microstructures in dark-colored domains at Punta Bianca observed **(a-b-c-d)** under crossed polarized light (CPL) and **(e-f-g-h)** with the retardation plate inserted (CPL+RP). **(a)**

General texture characterized by intergrowing decussate biotite grains, euhedral andalusite, and aggregates of K-feldspar, plagioclase, and quartz. The yellow rectangle highlights the location of Fig. 4d. **(b)** Foliated microstructure displaying subparallel biotite + ilmenite-, K-feldspar + plagioclase-, and quartz-rich layers. **(c)** K-feldspar + plagioclase + quartz-rich domain surrounding resorbed biotite grains. **(d)** Polygonal K-feldspar and quartz aggregate (white arrow) associated with misoriented biotite grains. **(e)** K-feldspar polycrystalline aggregate in contact with deformed quartz and biotite. The white arrow indicates an interstitial K-feldspar grain. **(f)** Orange-colored interstitial quartz with cuspate lobes (white arrows) surrounding rounded grains (yellow arrow) and euhedral grains (green arrow). Mineral abbreviations: And: andalusite; Bi: biotite; Cd: cordierite; Ilm: ilmenite; Ksp: K-feldspar; Pl: plagioclase; Q: quartz; Wm: white mica.

Figure 5 – Microstructures in light-colored domains at Punta Bianca. **(a)** Recrystallized quartz associated with elongated pseudomorphs of sericite over K-feldspar and plagioclase (CPL). **(b)** Recrystallized quartz-feldspar microstructure. Note the strongly elongated K-feldspar grains (CPL+RP). **(c)** Elongated K-feldspar + plagioclase aggregate (limits are contoured by the red dashed line) which follows a biotite-rich layer within quartz with amoeboid shape. The insert shows the resorbed outline of biotite (CPL). **(d)** Local polygonal texture with euhedral K-feldspar and quartz grain boundaries (red arrow) surrounded by interstitial K-feldspar with cuspate lobes (white arrows) (CPL+RP). Bi: biotite; Ilm: ilmenite; Ksp: K-feldspar; Pl: plagioclase; Q: quartz; Ser: sericite.

Figure 6 – Microstructures in dark-colored domains at Capo Calvo: **(a)** General microfabric showing biotite – andalusite – cordierite and K-feldspar and Note the strongly lobate shape of biotite in the insert (yellow box) of **(a)**. **(b)** Interstitial K-feldspar lobes against metamorphic quartz. The small K-feldspar grains (white arrows) are all in optical continuity (CPL + RP). **(c)** Interstitial K-feldspar surrounding strongly resorbed biotite grains (CPL). **(d)** Detail of the K-feldspar + plagioclase + quartz aggregates showing interstitial quartz or K-feldspar grains (white arrows) and crystal faces (red arrows) (CPL + RP). And: andalusite; Bi: biotite; Cd: cordierite; Ilm: ilmenite; Ksp: K-feldspar; Pl: plagioclase; Q: quartz; Ser: sericite.

Figure 7 – Microstructures in sample IESPCS42A, which is the representative of light-colored domains at Capo Calvo. **(a)** Thin section scan showing the relative area (in %) of the different mineral phases. See text for details. **(b)** Quartz grains with lobate boundaries, amoeboid shape and dissection microstructures (yellow arrow) (CPL). **(c)** Strongly lobate quartz grains showing pinning and window microstructures (white arrow). Biotite grains define the metamorphic foliation (CPL). **(d)** Pseudomorphed cordierite porphyroblasts surrounded by foliated quartz and biotite grains. SEM back scattered electron image. **(e)** K-feldspar-rich aggregate surrounded by quartz and biotite and characterized by a poikiloblastic microstructure due to biotite inclusions (CPL). Note the small K-feldspar lobes protruding in quartz (yellow arrows). Bi: biotite. Cd: cordierite. Ksp: K-feldspar. Pl: plagioclase. Q: quartz.

Figure 8 – Microstructures in sample IESPCS42A (continues). **(a)** BSE image of Fig. 7e showing the poikiloblastic microstructure of K-feldspar, related to resorbed (light blue arrow) and euhedral biotite inclusions (see insert). Note both the cuspate K-feldspar lobes (red arrows)

and the thin layer of K-feldspar following a biotite-rich layer in quartz (green arrow) (BSE). **(b)** Detail of the interstitial K-feldspar lobes (white arrows) occurring at the contact between feldspar aggregates and quartz (location in Fig. 8b). Feldspar is bluish whereas quartz is reddish (CPL + RP). **(c)** Interstitial K-feldspar showing lobate contacts with quartz and biotite. The red arrows mark feldspar lobes with very low apparent dihedral angle against quartz. Note the presence of crystal faces in quartz at the contact with K-feldspar (BSE). **(d)** Interstitial K-feldspar interposed between quartz and biotite and within biotite grains (BSE). **(e)** Crystal faces (white arrows) at the contact between euhedral to subhedral K-feldspar, quartz, and plagioclase grains (CPL + RP). **(f)** Feldspar grains showing rounded outline (light blue) surrounded by interstitial K-feldspar and plagioclase (orange – reddish) (CPL + RP). Bi: biotite; Ksp: K-feldspar; Pl: plagioclase; Q: quartz.

Figure 9 – Microstructures in schists associated to shear zones. **(a)** Photo stitching of a thin section of sample IESPSP196 (CPL). The different colors show the relative area % occupied by the phases present for shear zone (top) and wall rock (bottom) subdomains. **(b)** Quartz and biotite layers defining the foliation. Note the extensive recrystallization along quartz rims and undulose extinction in biotite (CPL). **(c)** Serrated quartz aggregates developed along grain boundaries of larger grains (CPL). **(d)** Sheared, poikiloblastic K-feldspar aggregates wrapped by biotite and quartz (CPL). **(e)** Detail of the strain caps surrounding feldspar aggregates (red arrow), characterized by recrystallized quartz and fine-grained white mica and biotite (CPL). Bi: biotite. Chl: chlorite Ksp: K-feldspar. Pl: plagioclase. Q: quartz. Wm: white mica.

Figure 10 – Microstructures in schists associated to shear zones (continues) **(a)** Interstitial quartz surrounding subhedral K-feldspar grains locally showing resorbed grain boundaries (CPL). **(b)** Crystal faces (red arrow) associated with more lobate boundaries between K-feldspar and quartz. Note the small K-feldspar inclusion (orange colors) with serrated grain boundaries (CPL + RP). **(c)** Recrystallized fine-grained K-feldspar ribbons being parallel to quartz layers. Note the mixing between K-feldspar and white mica in the upper-right corner (CPL). **(d)** Sericite-rich layers containing minor biotite and retrogressed cordierite, stretched parallel to the foliation. Scattered K-feldspar relics are present (CPL). Bi: biotite. Chl: chlorite. Ksp: K-feldspar. Pl: plagioclase. Q: quartz. Ser: sericite. Wm: white mica.

Figure 11 – Compositional maps of sample IESPCS42A. **(a-b)** BSE-Images showing the location of compositional maps on **(a)** resorbed biotite aligned on the foliation (X-Ray Map 1) and **(b)** resorbed and euhedral biotite included in poikiloblastic K-feldspar (X-Ray Map 2). **(c-d-e-f-g-h)** Compositional maps showing the distribution of **(c-f)** Fe, **(d-g)** Al, **(e-h)** and Ti in **(c-d-e)** X-Ray Map 1 and **(f-g-h)** X-Ray Map 2. See text for a detailed comment. Bi: biotite. Chl: chlorite. Ilm: ilmenite; Ksp: K-feldspar. Pl: plagioclase. Ser: sericite. Ru: rutile.

Figure 12 - (a) X_{Fe} – total Al^{IV} p.f.u. diagram showing the classification of the analyzed biotite, following Deer et al. (1992); **(b)** Compositional variability of biotite in the X_{Fe} – Ti p.f.u. space. **(c)** Results of Ti-in-biotite geothermometry based on the geothermometer by Wu and Chen (2015).

Figure 13 – P-T pseudosections of sample IESP3CS42A (microstructures in Fig. 7 and 8) modeled in the MnNCKFMASHT system. The subsolidus part was calculated assuming excess H_2O while the suprasolidus region was calculated with a fixed 1.66 mol% H_2O content (0.5 vol% of water at 0.2 GPa at the solidus). Quartz is present in all fields. X_{Fe} isopleths for biotite (yellow dashed lines) and cordierite (blue dashed lines) are shown. Black dashed lines are the melt isomodes. The red line marks the solidus. And: andalusite Bi: biotite. Cd: cordierite. Chl: chlorite. G: garnet. Ilm: ilmenite. Liq: melt. Mu: muscovite. Opx: orthopyroxene. Pl: plagioclase. Q: quartz. Sill: sillimanite. Ru: rutile.

Table captions

Table 1 – Radiometric ages in samples of metamorphic and igneous rocks from the Calamita peninsula, after a: Musumeci et al. (2011); b: Musumeci et al. (2015) and c: Viola et al. (2018). And = andalusite; Bi = biotite; Cd = cordierite; Di = diopside; Phl = phlogopite.

Table 2 – Representative analyses of biotite, pinitized cordierite, K-feldspar, plagioclase, ilmenite, and white mica in sample IESP3CS42A. T is the temperature estimated using the Ti-in-biotite geothermometer by Wu and Chen (2015). Ksp = K-feldspar. Ilm = ilmenite. Wm = white mica.

References

Barberi, F., Innocenti, F., Ricci, C.A., 1967. Il complesso scistoso di Capo Calamita (Isola d'Elba). *Atti della Società Toscana di Scienze Naturali residente a Pisa, Memorie, Serie A 72*, 579–617.

Barboni, M., Annen, C., Schoene, B., 2015. Evaluating the construction and evolution of upper crustal magma reservoirs with coupled U/Pb zircon geochronology and thermal modeling: A case study from the Mt. Capanne pluton (Elba, Italy). *Earth and Planetary Science Letters 432*, 436-448.

Bouillin J.P., Popeau G., Sabil N. 1994. Etude thermo-chronologique de la dénutation du pluton du Monte Capanne (ile d'Elbe, Italie) par le traces de fission. *Boll. Soc. Geol. France, 165*, 1, 19-25.

Brown, M., 2002. Retrograde processes in migmatites and granulites revisited. *Journal of Metamorphic Geology 20*, 25-40.

Brown, M., 2010. Melting of the continental crust during orogenesis: the thermal, rheological, and compositional consequences of melt transport from lower to upper continental crust. *Canadian Journal of Earth Sciences 47*, 655-694.

Buick, I. S., Stevens, G., Gibson, R. L., 2004. The role of water retention in the anatexis of metapelites in the Bushveld Complex Aureole, South Africa: an experimental study. *Journal of Petrology 45*(9), 1777-1797.

Cesare, B., Marchesi, C., Hermann, J., Gómez-Pugnaire, M. T., 2003. Primary melt inclusions in andalusite from anatectic graphitic metapelites: implications for the position of the Al2SiO5 triple point. *Geology 31*(7), 573-576.

Coggon, R., Holland, T. J. B., 2002. Mixing properties of phengitic micas and revised garnet-phengite thermobarometers. *Journal of Metamorphic Geology 20*, 683-696.

Cooper, R. F., Kohlstedt, D. L., 1984. Solution-precipitation enhanced diffusional creep of partially molten olivine-basalt aggregates during hot-pressing. *Tectonophysics 107*, 207-233.

Davidson, C., Schmid, S. M., Hollister, L. S., 1994. Role of melt during deformation in the deep crust. *Terra Nova 6*, 133-142.

Deer, W., Howie, R., Zussman, J., 1992. *An Introduction to the Rock-forming Minerals*, second ed. Pearson Education Ltd., Harlow, England.

Dell'Angelo, L. N., Tullis, J., 1988. Experimental deformation of partially melted granitic aggregates. *Journal of Metamorphic Geology 6*, 495-515.

Dell'Angelo, L. N., Tullis, J., Yund, R. A., 1987. Transition from dislocation creep to melt-enhanced diffusion creep in fine-grained granitic aggregates. *Tectonophysics 139*, 325-332.

Diener, J. F., Fagereng, Å., 2014. The influence of melting and melt drainage on crustal rheology during orogenesis. *Journal of Geophysical Research: Solid Earth 119*, 6193-6210.

Diener, J. F. A., Powell, R., White, R. W., Holland, T. J. B., 2007. A new thermodynamic model for clino- and orthoamphiboles in the system Na2O–CaO–FeO–MgO–Al2O3–SiO2–H2O–O. *Journal of Metamorphic Geology 25*, 631-656.

Diener, J. F., Fagereng, Å., Thomas, S. A., 2016. Mid-crustal shear zone development under retrograde conditions: pressure–temperature–fluid constraints from the Kuckaus Mylonite Zone, Namibia. *Solid Earth 7*, 1331-1347.

Dini, A., Innocenti, F., Rocchi, S., Tonarini, S., Westerman, D. S., 2002. The magmatic evolution of the late Miocene laccolith–pluton–dyke granitic complex of Elba Island, Italy. *Geological Magazine 139*, 257-279.

Droop, G. T. R., Brodie, K. H., 2012. Anatectic melt volumes in the thermal aureole of the Etive Complex, Scotland: the roles of fluid-present and fluid-absent melting. *Journal of Metamorphic Geology 30*, 843-864.

Duranti, S., Palmeri, R., Pertusati, P. C., Ricci, C. A., 1992. Geological evolution and metamorphic petrology of the basal sequences of eastern Elba (complex II). *Acta Vulcanologica 2*, 213-229.

Gapais, D., 1989. Shear structures within deformed granites: mechanical and thermal indicators. *Geology 17*(12), 1144-1147.

Guernina, S., Sawyer, E. W., 2003. Large-scale melt-depletion in granulite terranes: an example from the Archean Ashuanipi Subprovince of Quebec. *Journal of Metamorphic Geology 21*, 181-201.

Henry, D. J., Guidotti, C. V., Thomson, J. A., 2005. The Ti-saturation surface for low-to-medium pressure metapelitic biotites: Implications for geothermometry and Ti-substitution mechanisms. *American Mineralogist 90*(2-3), 316-328.

Hippertt, J. F., Hongn, F. D., 1998. Deformation mechanisms in the mylonite/ultramylonite transition. *Journal of Structural Geology 20*, 1435-1448.

Hippertt, J., Rocha, A., Lana, C., Egydio-Silva, M., Takeshita, T., 2001. Quartz plastic segregation and ribbon development in high-grade striped gneisses. *Journal of Structural Geology 23*(1), 67-80.

Holland, T. J. B., Powell, R., 1998. An internally consistent thermodynamic data set for phases of petrological interest. *Journal of Metamorphic Geology 16*, 309-343.

Holland, T., Powell, R., 2003. Activity–composition relations for phases in petrological calculations: an asymmetric multicomponent formulation. *Contributions to Mineralogy and Petrology 145*, 492-501.

Hollister, L. S., Crawford, M. L., 1986. Melt-enhanced deformation: A major tectonic process. *Geology 14*, 558-561.

Holness, M. B., Clemens, J. D., 1999. Partial melting of the Appin quartzite driven by fracture-controlled H_2O infiltration in the aureole of the Ballachulish Igneous Complex, Scottish Highlands. *Contributions to Mineralogy and Petrology 136*, 154-168.

Holness, M. B., Sawyer, E. W., 2008. On the pseudomorphing of melt-filled pores during the crystallization of migmatites. *Journal of Petrology 49*, 1343-1363.

Holness, M. B., Cesare, B., Sawyer, E. W., 2011. Melted rocks under the microscope: microstructures and their interpretation. *Elements 7*(4), 247-252.

Holyoke III, C. W., Tullis, J. 2006. The interaction between reaction and deformation: an experimental study using a biotite + plagioclase + quartz gneiss. *Journal of Metamorphic Geology 24*(8), 743-762.

Jessell, M. W., 1987. Grain-boundary migration microstructures in a naturally deformed quartzite. *Journal of Structural Geology 9*, 1007-1014.

Johnson, T. E., Gibson, R. L., Brown, M., Buick, I. S., Cartwright, I. A. N., 2003. Partial melting of metapelitic rocks beneath the Bushveld Complex, South Africa. *Journal of Petrology 44*, 789-813.

Karlstrom, K. E., Miller, C. F., Kingsbury, J. A., Wooden, J. L., 1993. Pluton emplacement along an active ductile thrust zone, Piute Mountains, southeastern California: Interaction between deformational and solidification processes. *Geological Society of America Bulletin 105*, 213-230.

Keller, J. V. A., Coward, M. P., 1996. The structure and evolution of the Northern Tyrrhenian Sea. *Geological Magazine 133*, 1-16.

Kruckenberg, S.C., Vanderhaeghe, O., Ferré, E.C., Teyssier, C., Whitney, D.L., 2011. Flow of partially molten crust and the internal dynamics of a migmatite dome, Naxos, Greece. *Tectonics 30*.

Le Breton, N., Thompson, A. B., 1988. Fluid-absent (dehydration) melting of biotite in metapelites in the early stages of crustal anatexis. *Contributions to Mineralogy and Petrology 99*, 226-237.

Luan, F. C., Paterson, M. S., 1992. Preparation and deformation of synthetic aggregates of quartz. *Journal of Geophysical Research: Solid Earth 97*(B1), 301-320.

Mahar, E. M., Baker, J. M., Powell, R., Holland, T. J. B., Howell, N., 1997. The effect of Mn on mineral stability in metapelites. *Journal of Metamorphic Geology 15*, 223-238.

Marchildon, N., Brown, M., 2002. Grain-scale melt distribution in two contact aureole rocks: Implications for controls on melt localization and deformation. *Journal of Metamorphic Geology 20*, 381-396.

Mariani, E., Brodie, K. H., Rutter, E. H., 2006. Experimental deformation of muscovite shear zones at high temperatures under hydrothermal conditions and the strength of phyllosilicate-bearing faults in nature. *Journal of Structural Geology 28*, 1569-1587.

Massa, G., Musumeci, G., Mazzarini, F., Pieruccioni, D., 2017. Coexistence of contractional and extensional tectonics during the northern Apennines orogeny: the late Miocene out-of-sequence thrust in the Elba Island nappe stack. *Geological Journal 52*, 353-368.

Mazzarini, F., Musumeci, G., Cruden, A. R., 2011. Vein development during folding in the upper brittle crust: The case of tourmaline-rich veins of eastern Elba Island, northern Tyrrhenian Sea, Italy. *Journal of Structural Geology 33*, 1509-1522.

Miranda, E. A., Klepeis, K. A., 2016. The interplay and effects of deformation and crystallized melt on the rheology of the lower continental crust, Fiordland, New Zealand. *Journal of Structural Geology 93*, 91-105.

Misra, S., Burg, J. P., Vigneresse, J. L., Mainprice, D., 2014. Rheological transition during large strain deformation of melting and crystallizing metapelites. *Journal of Geophysical Research: Solid Earth 119*, 3971-3985.

Mitra, G., 1978. Ductile deformation zones and mylonites; the mechanical processes involved in the deformation of crystalline basement rocks. *American Journal of Science 278*, 1057-1084.

Musumeci, G., Vaselli, L., 2012. Neogene deformation and granite emplacement in the metamorphic units of northern Apennines (Italy): Insights from mylonitic marbles in the Porto Azzurro pluton contact aureole (Elba Island). *Geosphere 8*, 470-490.

Musumeci, G., Mazzarini, F., Tiepolo, M., Di Vincenzo, G., 2011. U-Pb and 40Ar-39Ar geochronology of Palaeozoic units in the northern Apennines: determining protolith age and alpine evolution using the Calamita Schist and Ortano Porphyroid. *Geological Journal 46*, 288-310.

Musumeci, G., Mazzarini, F., Cruden, A. R., 2015. The Zuccale Fault, Elba Island, Italy: a new perspective from fault architecture. *Tectonics 34*, 1195-1218.

Papeschi, S., Musumeci, G., 2019. Fluid assisted strain localization in quartz at the brittle/ductile transition. *Geochemistry, Geophysics, Geosystems 20*, 3044-3064.

Papeschi, S., Musumeci, G., Mazzarini, F., 2017. Heterogeneous brittle-ductile deformation at shallow crustal levels under high thermal conditions: The case of a synkinematic contact aureole in the inner northern Apennines, southeastern Elba Island, Italy. *Tectonophysics 717*, 547-564.

Papeschi, S., Musumeci, G., Mazzarini, F., 2018. Evolution of shear zones through the brittle-ductile transition: The Calamita Schists (Elba Island, Italy). *Journal of Structural Geology 113*, 100-114.

Passchier, C. W., Trouw, R. A. 2005. *Microtectonics*. Springer Science & Business Media.

Pattison, D. R. M., Harte, B., 1988. Evolution of structurally contrasting anatectic migmatites in the 3 kbar Ballachulish aureole, Scotland. *Journal of Metamorphic Geology 6*, 475-494.

Pawley, M. J., Collins, W. J., 2002. The development of contrasting structures during the cooling and crystallisation of a syn-kinematic pluton. *Journal of Structural Geology 24*(3), 469-483.

Platten, I.M., 1982. Partial melting of feldspathic quartzite around late Caledonian minor intrusion in Appin, Scotland. *Geological Magazine* 119, 413-419.

Post, A., Tullis, J., 1998. The rate of water penetration in experimentally deformed quartzite: implications for hydrolytic weakening. *Tectonophysics 295*, 117-137.

Powell, R., Holland, T. J. B., 1988. An internally consistent dataset with uncertainties and correlations: 3. Applications to geobarometry, worked examples and a computer program. *Journal of Metamorphic Geology 6*, 173-204.

Rosenberg, C. L., 2001. Deformation of partially molten granite: a review and comparison of experimental and natural case studies. *International Journal of Earth Sciences 90*(1), 60-76.

Rosenberg, C. L., Handy, M. R., 2000. Syntectonic melt pathways during simple shearing of a partially molten rock analogue (Norcamphor-Benzamide). *Journal of Geophysical Research: Solid Earth 105*(B2), 3135-3149.

Rosenberg, C. L., Handy, M. R., 2005. Experimental deformation of partially melted granite revisited: implications for the continental crust. *Journal of Metamorphic Geology 23*, 19-28.

Rutter, E. H., Neumann, D. H. K., 1995. Experimental deformation of partially molten Westerly granite under fluid-absent conditions, with implications for the extraction of granitic magmas. *Journal of Geophysical Research: Solid Earth 100*, 15697-15715.

Sawyer, E. W, 1999. Criteria for the recognition of partial melting. *Physics and Chemistry of the Earth, Part A: Solid Earth and Geodesy 24*, 269-279.

Sawyer, E. W., 2001. Melt segregation in the continental crust: distribution and movement of melt in anatectic rocks. *Journal of Metamorphic Geology 19*(3), 291-309.

Sawyer, E. W., 2008. Atlas of migmatites. The Canadian Mineralogist, Special Publication 9. NRC Research Press, Ottawa, Ontario, Canada.

Schneider, C. A., Rasband, W. S., Eliceiri, K. W., 2012. NIH Image to ImageJ: 25 years of image analysis. *Nature Methods 9*, 671.

Schulmann, K., Martelat, J. E., Ulrich, S., Lexa, O., Štípská, P., Becker, J. K., 2008. Evolution of microstructure and melt topology in partially molten granitic mylonite: Implications for rheology of felsic middle crust. *Journal of Geophysical Research: Solid Earth 113*(B10).

Stipp, M., Stünitz, H., Heilbronner, R., Schmid, S. M., 2002. The eastern Tonale fault zone: a 'natural laboratory' for crystal plastic deformation of quartz over a temperature range from 250 to 700 °C. *Journal of Structural Geology 24*, 1861-1884.

Stuart, C. A., Piazolo, S., Daczko, N. R., 2018. The recognition of former melt flux through high-strain zones. *Journal of Metamorphic Geology 36*, 1049-1069.

Stünitz, H., Tullis, J., 2001. Weakening and strain localization produced by syn-deformational reaction of plagioclase. *International Journal of Earth Sciences 90*, 136-148.

Tullis, J., Stünitz, H., Teyssier, C., Heilbronner, R., 2000. Deformation microstructures in quartzo-feldspathic rocks. In: Jessel, M. W., Urai, J. L. (Eds.) Stress, strain and structure, a volume in honour of W.D Means. *Journal of the Virtual Explorer, 2*.

Urai, J. L., Means, W. D., Lister, G. S., 1986. Dynamic recrystallization of minerals. *Mineral and Rock Deformation: Laboratory Studies,* AGU Geophysical Monograph Series 36, 161-199.

Vanderhaeghe, O., 2009. Migmatites, granites and orogeny: Flow modes of partially-molten rocks and magmas associated with melt/solid segregation in orogenic belts. *Tectonophysics 477*, 119-134.

Vernon, R. H., Clarke, G. L., 2008. *Principles of Metamorphic Petrology*. Cambridge University Press, Cambridge, England.

Vernon, R. H., Flood, R. H., 1987. Contrasting deformation and metamorphism of S and I type granitoids in the Lachian Fold Belt, Eastern Australia. *Tectonophysics 147*, 127-143.

Viegas, G., Menegon, L., Archanjo, C., 2016. Brittle grain-size reduction of feldspar, phase mixing and strain localization in granitoids at mid-crustal conditions (Pernambuco shear zone, NE Brazil). *Solid Earth 7*(2), 375-396.

Vielzeuf, D., Holloway, J. R., 1988. Experimental determination of the fluid-absent melting relations in the pelitic system. *Contributions to Mineralogy and Petrology 98*, 257-276.

Vigneresse, J. L., Tikoff, B., 1999. Strain partitioning during partial melting and crystallizing felsic magmas. *Tectonophysics 312*, 117-132.

Vigneresse, J. L., Barbey, P., Cuney, M., 1996. Rheological transitions during partial melting and crystallization with application to felsic magma segregation and transfer. *Journal of Petrology 37*, 1579-1600.

Viola, G., Torgersen, E., Mazzarini, F., Musumeci, G., van der Lelij, R., Schönenberger, J., Garofalo, P. S., 2018. New Constraints on the Evolution of the Inner Northern Apennines by K-Ar Dating of Late Miocene-Early Pliocene Compression on the Island of Elba, Italy. *Tectonics 37*, 3229-3243.

Walte, N. P., Bons, P. D., Passchier, C. W., 2005. Deformation of melt-bearing systems—insight from in situ grain-scale analogue experiments. *Journal of Structural Geology 27*(9), 1666-1679.

White, S. H., Burrows, S. E., Carreras, J., Shaw, N. D., Humphreys, F. J., 1980. On mylonites in ductile shear zones. *Journal of Structural Geology 2*, 175-187.

White, R. W., Powell, R., 2002. Melt loss and the preservation of granulite facies mineral assemblages. *Journal of Metamorphic Geology 20*, 621-632.

White, R. W., Powell, R., Holland, T. J. B., Worley, B. A., 2000. The effect of TiO_2 and Fe_2O_3 on metapelitic assemblages at greenschist and amphibolite facies conditions: mineral equilibria calculations in the system K_2O-FeO-MgO-Al_2O_3-SiO_2-H_2O-TiO_2-Fe_2O_3. *Journal of Metamorphic Geology 18*, 497-511.

White, R. W., Powell, R., Clarke, G. L., 2002. The interpretation of reaction textures in Fe-rich metapelitic granulites of the Musgrave Block, central Australia: constraints from mineral equilibria calculations in the system K_2O-FeO-MgO-Al_2O_3-SiO_2-H_2O-TiO_2-Fe_2O_3. *Journal of Metamorphic Geology 20*, 41-55.

White, R. W., Pomroy, N. E., Powell, R., 2005. An in situ metatexite–diatexite transition in upper amphibolite facies rocks from Broken Hill, Australia. *Journal of Metamorphic Geology 23*, 579-602.

White, R. W., Powell, R., Holland, T. J. B., 2007. Progress relating to calculation of partial melting equilibria for metapelites. *Journal of Metamorphic Geology 25*, 511-527.

Wu, C. M., Chen, H. X., 2015. Revised Ti-in-biotite geothermometer for ilmenite- or rutile-bearing crustal metapelites. *Science Bulletin 60*(1), 116-121.

Yakymchuk, C., Brown, M., 2014. Consequences of open-system melting in tectonics. *Journal of the Geological Society 171*, 21-40.

Závada, P., Schulmann, K., Konopásek, J., Ulrich, S., Lexa, O., 2007. Extreme ductility of feldspar aggregates—Melt-enhanced grain boundary sliding and creep failure: Rheological implications for felsic lower crust. *Journal of Geophysical Research: Solid Earth 112*.

Zibra, I., White, J. C., Menegon, L., Dering, G., Gessner, K., 2018. The ultimate fate of a synmagmatic shear zone. Interplay between rupturing and ductile flow in a cooling granite pluton. *Journal of Structural Geology 110*, 1-23.

Table 1 – Radiometric ages in samples of metamorphic and igneous rocks from the Calamita peninsula, after a: Musumeci et al. (2011); b: Musumeci et al. (2015) and c: Viola et al. (2018). And = andalusite; Bi = biotite; Cd = cordierite; Di = diopside; Phl = phlogopite.

Rock type	Phase dated	Method	Age (Ma)
And-Cd-Bi schist	biotite	$^{40}Ar/^{39}Ar$	6.23±0.06 Ma[a]
And-Cd-Bi schist	zircon	U/Pb	6.40±0.15 Ma[a]
Di-Phl marble	phlogopite	$^{40}Ar/^{39}Ar$	6.76±0.08 Ma[b]
Leucogranite	white mica	$^{40}Ar/^{39}Ar$	6.33±0.07 Ma[b]
Mylonite	authigenic illite	K/Ar	6.14±0.64 Ma[c]
Fault gouge (CN-MAT)	authigenic illite	K/Ar	4.90±0.27 Ma[c]

Table 2 – Representative analyses of biotite, pinitized cordierite, K-feldspar, plagioclase, ilmenite and white mica in sample IESP3CS42A. T is the temperature estimated using the Ti-in-biotite geothermometer by Wu & Chen (2015). Ksp = K-feldspar. Ilm = ilmenite. Wm = white mica.

	Biotite							Cordierite (pinitized)		K-feldspar		Plagioclase		Ilm	Wm
	Resorbed				Euhedral, in Ksp		Retro grade								Retro grade
	core		rim												
Analysis	2	5	8	54	23	25	85a	1a	16a	22	48	46	102	83a	100a
SiO_2	33.62	33.29	33.56	34.10	33.83	34.43	35.83	44.21	45.25	60.88	63.42	65.45	66.14	0.04	46.90
TiO_2	2.02	2.10	3.19	2.90	1.84	1.85	0.83	0.04	0.00	0.00	0.00	0.04	0.00	50.79	0.14
Al_2O_3	18.50	18.16	17.51	18.29	18.35	18.70	16.87	29.57	29.98	17.42	18.30	21.14	22.55	0.00	31.54
FeOtot	23.34	23.40	22.23	23.01	22.13	20.83	18.98	6.47	7.77	1.61	0.24	0.41	0.04	40.31	1.82
MnO	0.07	0.13	0.04	0.05	0.06	0.05	0.06	0.00	0.00	0.00	0.00	0.00	0.01	3.89	0.02
MgO	6.80	6.79	6.92	6.78	7.02	7.38	10.81	3.44	3.54	1.14	0.14	0.00	0.00	0.03	1.23
CaO	0.02	0.02	0.00	0.05	0.01	0.08	0.00	0.09	0.00	0.04	0.05	2.50	3.31	0.06	0.04
BaO	0.11	0.04	0.09	0.12	0.06	0.10	0.00	0.13	0.02	0.71	0.87	0.00	0.00	0.00	0.11
Na_2O	0.22	0.22	0.17	0.17	0.15	0.13	0.05	0.20	0.20	0.51	0.64	9.99	8.58	0.00	0.21
K_2O	8.91	9.02	9.47	9.19	9.06	9.16	9.85	10.82	10.84	14.79	14.86	0.26	0.22	0.01	10.46
Total	93.61	93.17	93.17	94-66	92.50	92.72	93.27	94.97	97.59	97.09	98.52	99.78	100.8	96.99	92.48
Si	5.33	5.32	5.35	5.34	5.40	5.44	5.59	5.02	5.02	2.94	2.98	2.89	2.87	0.00	3.22
Al	3.46	3.42	3.29	3.38	3.45	3.52	3.10	3.96	3.92	0.99	1.01	1.10	1.15	0.00	2.56
Ti	0.24	0.25	0.38	0.34	0.22	0.22	0.10	0.00	0.00	0.00	0.00	0.00	0.00	1.01	0.01
Fe^{2+}_{TOT}	3.10	3.13	2.96	3.01	2.95	2.75	2.48	0.61	0.72	0.06	0.01	0.02	0.00	0.89	0.10
Mn	0.01	0.02	0.00	0.01	0.01	0.01	0.01	0.00	0.00	0.00	0.00	0.00	0.00	0.09	0.00
Mg	1.61	1.62	1.64	1.58	1.67	1.74	2.51	0.58	0.58	0.08	0.01	0.00	0.00	0.00	0.13
Ca	0.00	0.00	0.00	0.01	0.00	0.01	0.00	0.01	0.00	0.00	0.00	0.12	0.15	0.00	0.00
Ba	0.01	0.00	0.01	0.01	0.00	0.01	0.00	0.01	0.00	0.01	0.02	0.00	0.00	0.00	0.00
Na	0.07	0.07	0.05	0.05	0.05	0.04	0.02	0.04	0.04	0.05	0.06	0.85	0.72	0.00	0.03
K	1.80	1.84	1.93	1.84	1.85	1.85	1.96	1.57	1.53	0.91	0.89	0.01	0.01	0.00	0.92
T(°C)	591	594	650	644	575	573	423	-	-	-	-	-	-	-	-

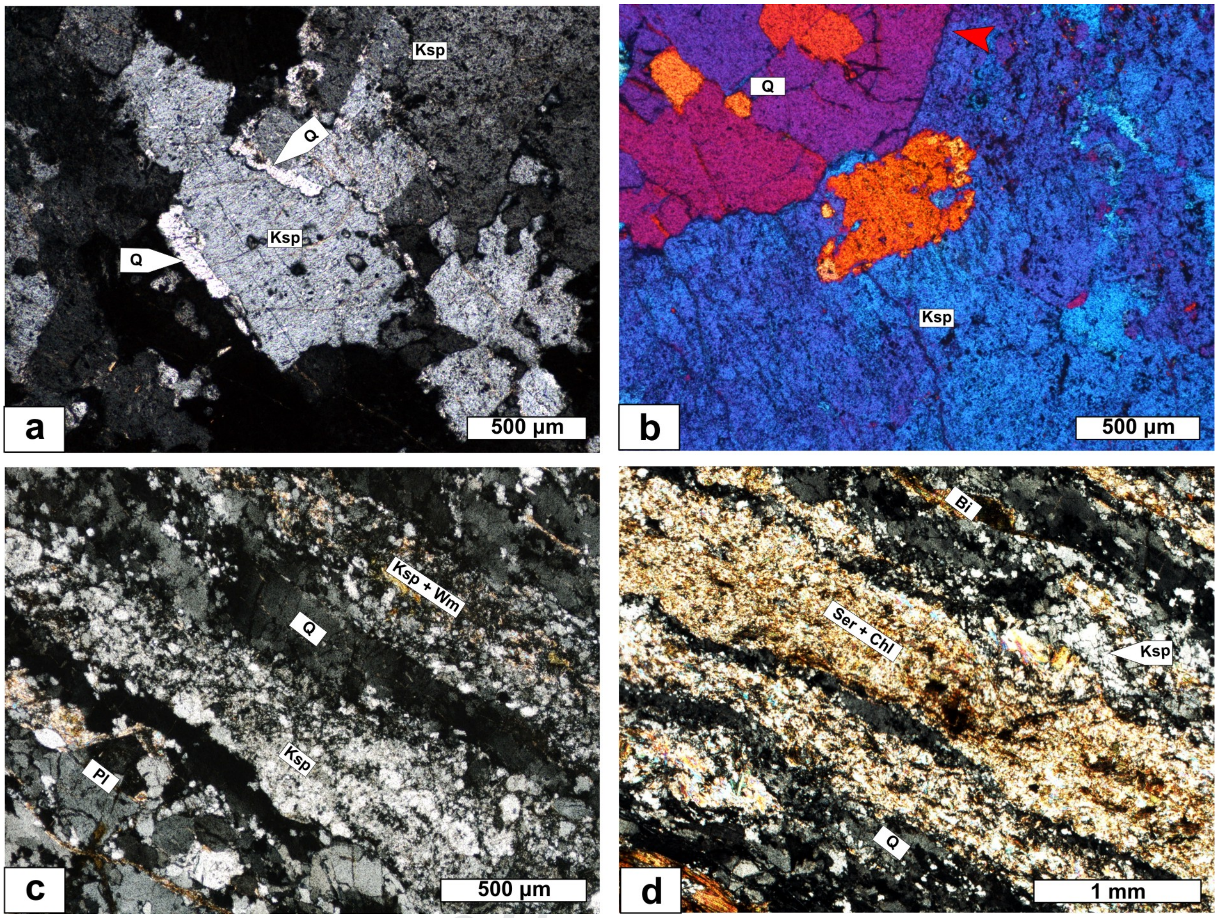
Ksp
Q
Ksp
Q
a
500 µm
Q
Ksp
b
500 µm
Ksp + Wm
Q
Ksp
Pl
c
500 µm
Bi
Ser + Chl
Ksp
Q
d
1 mm

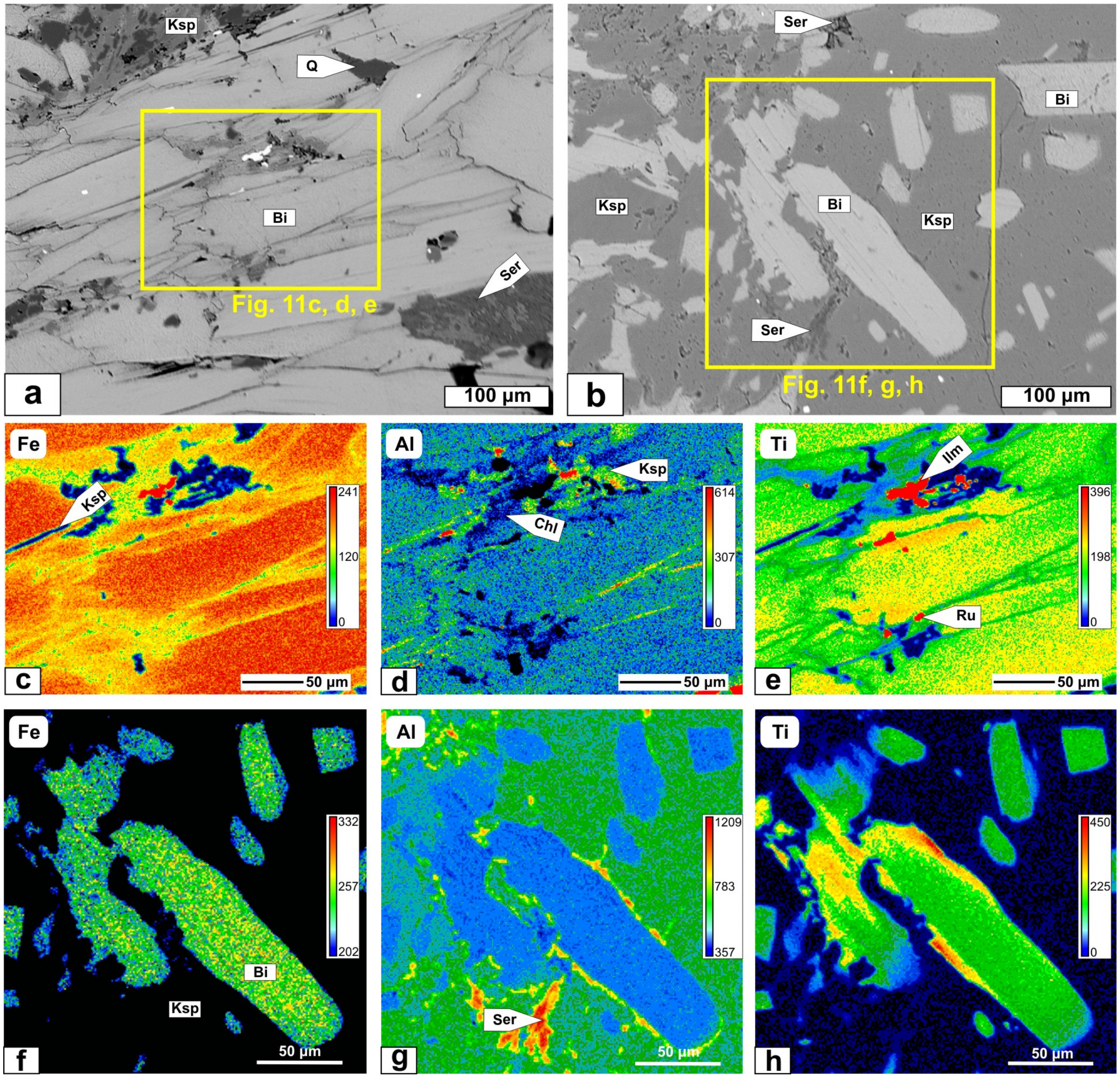

Ksp
Q
Bi
Ser
Fig. 11c, d, e
a
100 µm
Ser
Bi
Ksp
Bi
Ksp
Ser
Fig. 11f, g, h
b
100 µm
Fe
Ksp
241
120
0
c
50 µm
Al
Ksp
Chl
614
307
0
d
50 µm
Ti
Ilm
396
198
0
Ru
e
50 µm
Fe
332
257
202
Bi
Ksp
f
50 µm
Al
1209
783
357
Ser
g
50 µm
Ti
450
225
0
h
50 µm

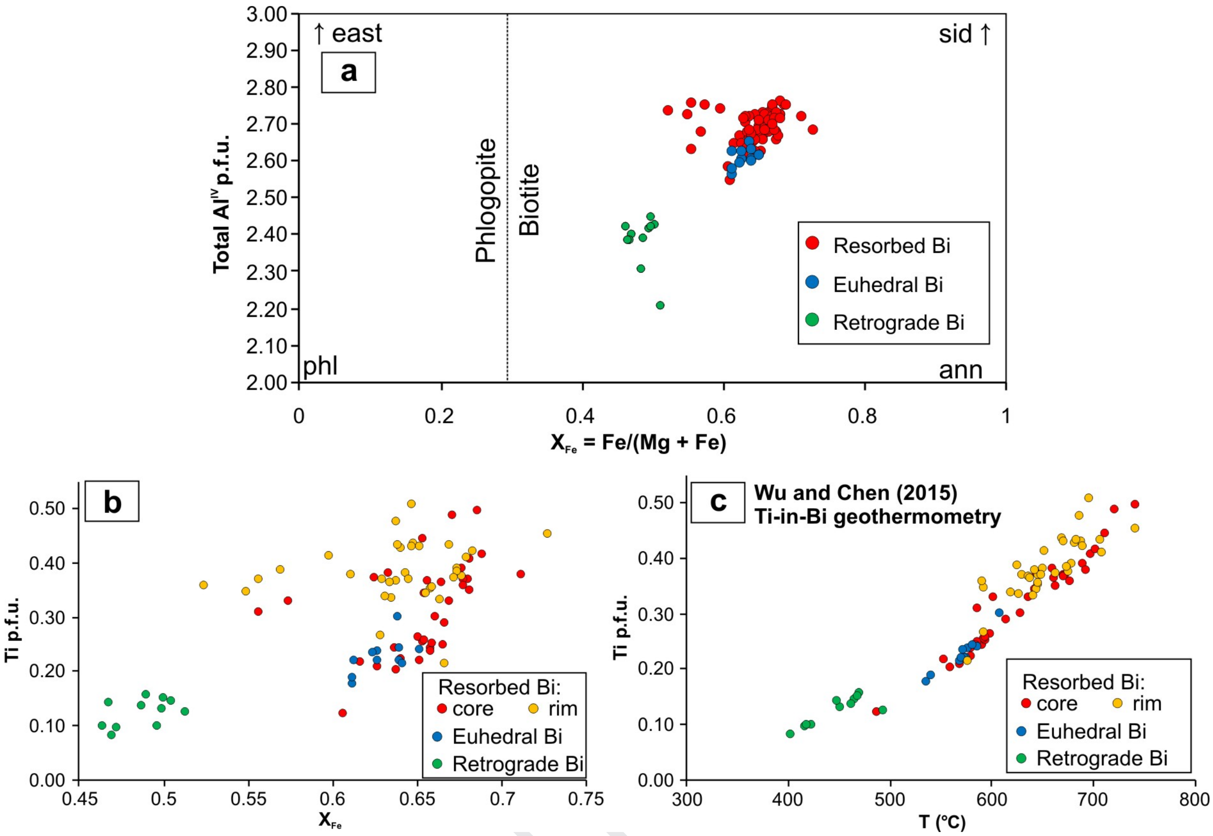

a
↑ east
sid ↑
phl
ann
Phlogopite
Biotite
Total Al^{IV} p.f.u.
X_{Fe} = Fe/(Mg + Fe)
Resorbed Bi
Euhedral Bi
Retrograde Bi
b
Ti p.f.u.
X_{Fe}
Resorbed Bi:
core
rim
Euhedral Bi
Retrograde Bi
c
Wu and Chen (2015)
Ti-in-Bi geothermometry
Ti p.f.u.
T (°C)

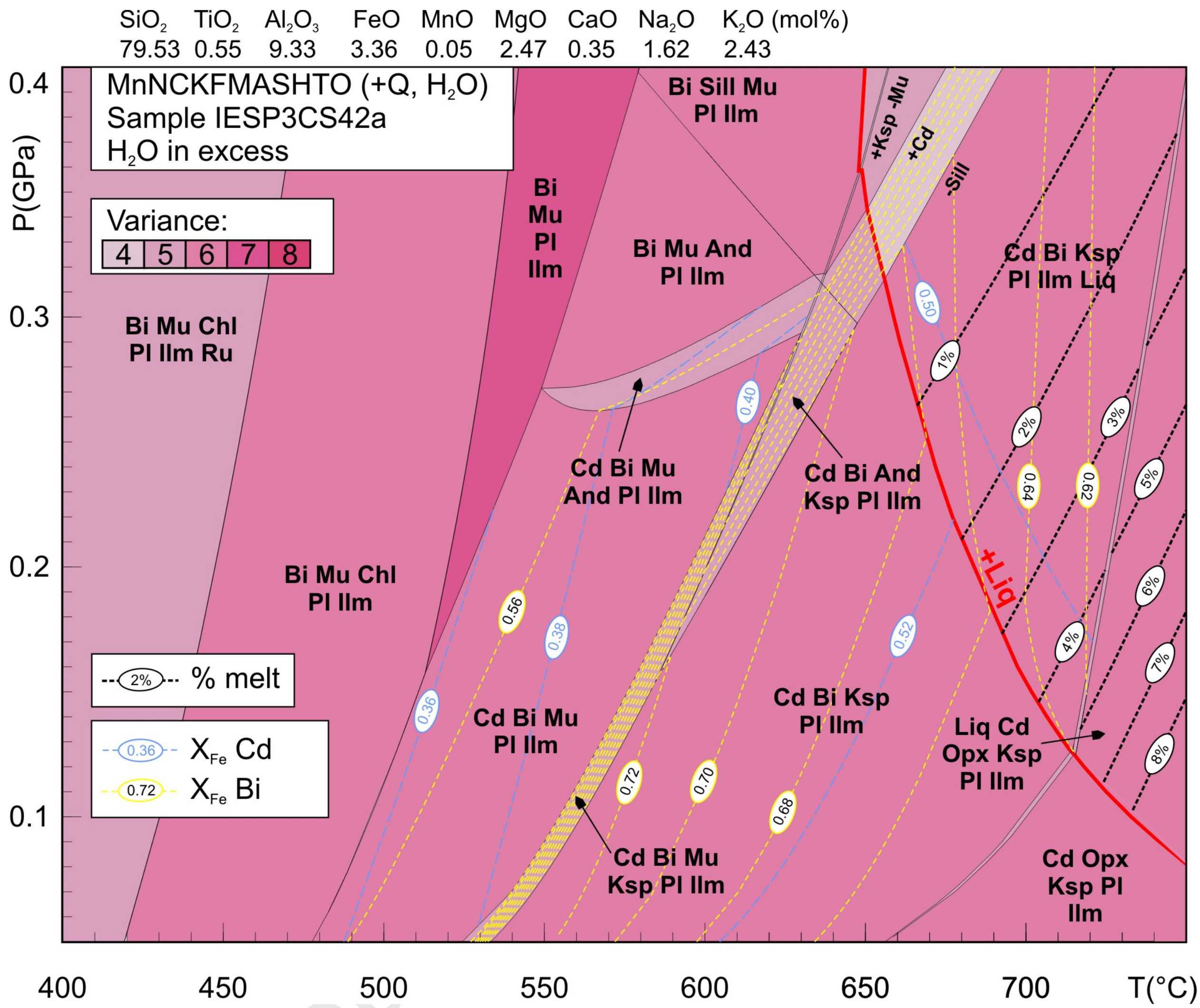

SiO2 TiO2 Al2O3 FeO MnO MgO CaO Na2O K2O (mol%)
79.53 0.55 9.33 3.36 0.05 2.47 0.35 1.62 2.43
MnNCKFMASHTO (+Q, H2O)
Sample IESP3CS42a
H2O in excess
Variance:
4 5 6 7 8
Bi Mu Chl Pl Ilm Ru
Bi Mu Chl Pl Ilm
Bi Mu Pl Ilm
Bi Sill Mu Pl Ilm
Bi Mu And Pl Ilm
Cd Bi Mu And Pl Ilm
Cd Bi And Ksp Pl Ilm
Cd Bi Mu Pl Ilm
Cd Bi Mu Ksp Pl Ilm
Cd Bi Ksp Pl Ilm
Cd Bi Ksp Pl Ilm Liq
Liq Cd Opx Ksp Pl Ilm
Cd Opx Ksp Pl Ilm
+Ksp -Mu
+Cd
-Sill
+Liq
% melt
XFe Cd
XFe Bi
P(GPa)
T(°C)

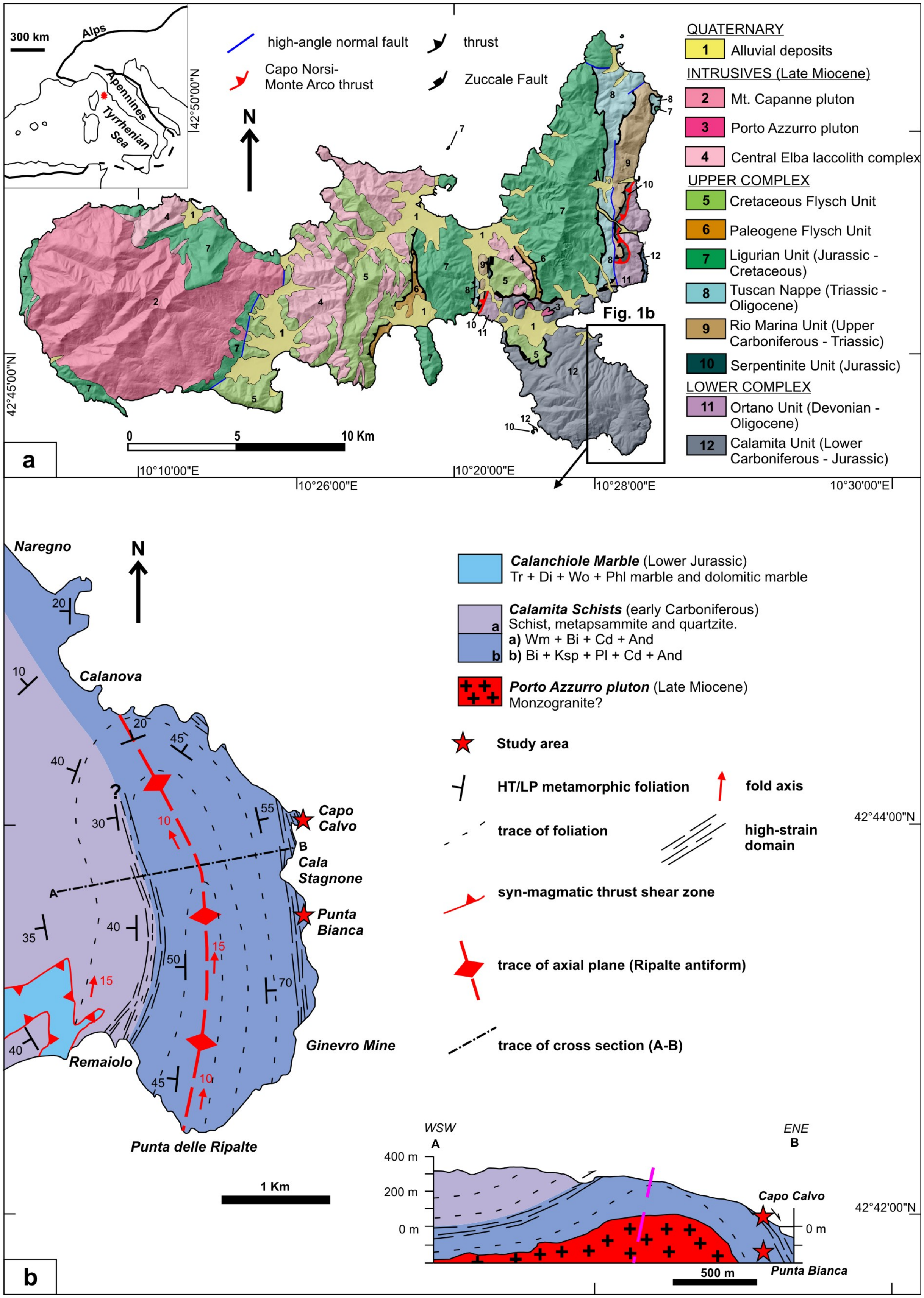

a
300 km
Alps
Apennines
Tyrrhenian Sea
high-angle normal fault
Capo Norsi-Monte Arco thrust
thrust
Zuccale Fault
N
Fig. 1b
0 5 10 Km
42°50'00"N
42°45'00"N
10°10'00"E
10°20'00"E
QUATERNARY
1 Alluvial deposits
INTRUSIVES (Late Miocene)
2 Mt. Capanne pluton
3 Porto Azzurro pluton
4 Central Elba laccolith complex
UPPER COMPLEX
5 Cretaceous Flysch Unit
6 Paleogene Flysch Unit
7 Ligurian Unit (Jurassic - Cretaceous)
8 Tuscan Nappe (Triassic - Oligocene)
9 Rio Marina Unit (Upper Carboniferous - Triassic)
10 Serpentinite Unit (Jurassic)
LOWER COMPLEX
11 Ortano Unit (Devonian - Oligocene)
12 Calamita Unit (Lower Carboniferous - Jurassic)
b
10°26'00"E
10°28'00"E
10°30'00"E
42°44'00"N
42°42'00"N
Naregno
Calanova
Capo Calvo
Cala Stagnone
Punta Bianca
Ginevro Mine
Remaiolo
Punta delle Ripalte
1 Km
Calanchiole Marble (Lower Jurassic)
Tr + Di + Wo + Phl marble and dolomitic marble
Calamita Schists (early Carboniferous)
Schist, metapsammite and quartzite.
a) Wm + Bi + Cd + And
b) Bi + Ksp + Pl + Cd + And
Porto Azzurro pluton (Late Miocene)
Monzogranite?
Study area
HT/LP metamorphic foliation
fold axis
trace of foliation
high-strain domain
syn-magmatic thrust shear zone
trace of axial plane (Ripalte antiform)
trace of cross section (A-B)
WSW
A
ENE
B
400 m
200 m
0 m
Capo Calvo
Punta Bianca
500 m

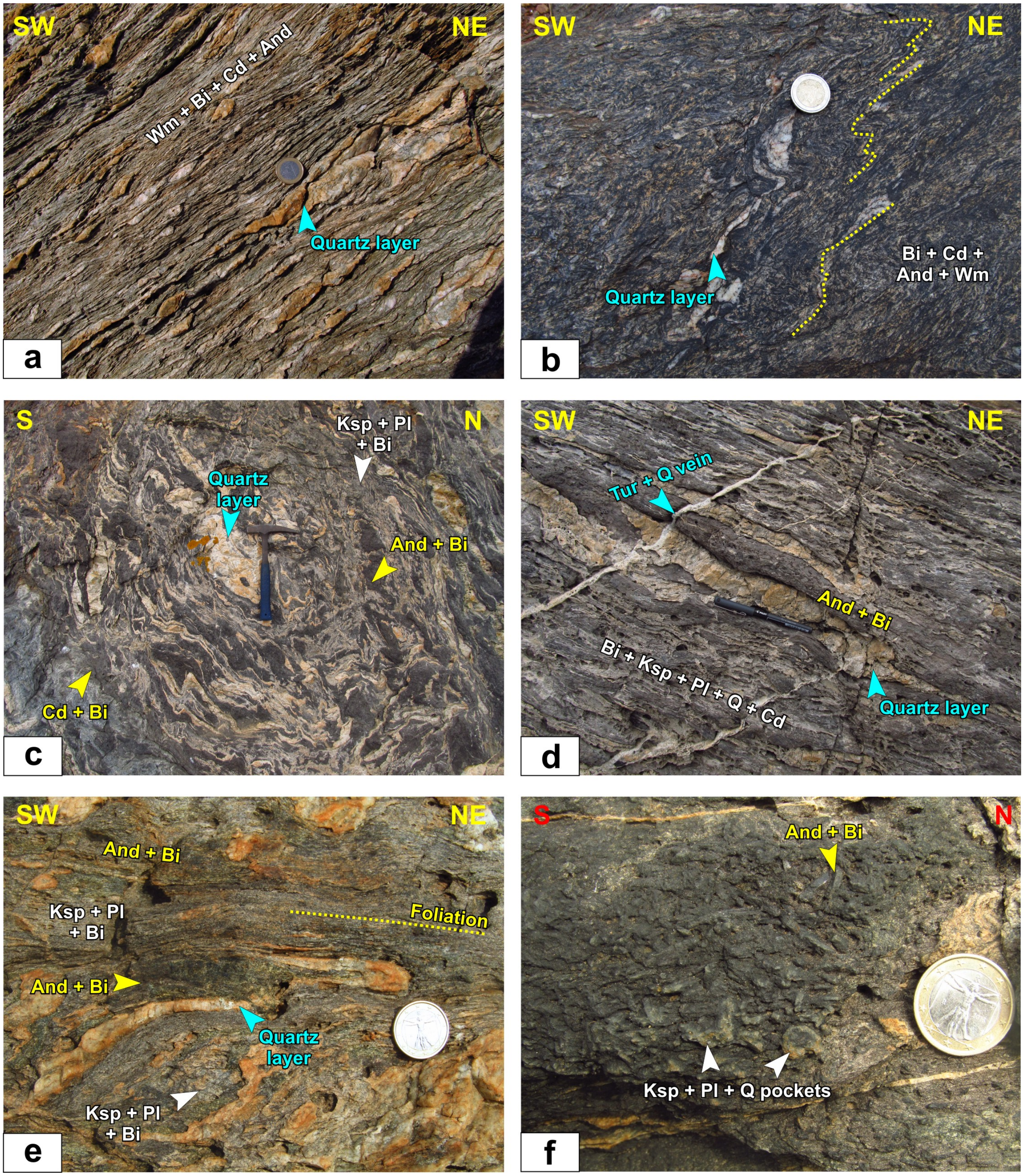
SW
NE
Wm + Bi + Cd + And
Quartz layer
a
SW
NE
Quartz layer
Bi + Cd +
And + Wm
b
S
N
Ksp + Pl
+ Bi
Quartz
layer
And + Bi
Cd + Bi
c
SW
NE
Tur + Q vein
And + Bi
Bi + Ksp + Pl + Q + Cd
Quartz layer
d
SW
NE
And + Bi
Ksp + Pl
+ Bi
Foliation
And + Bi
Quartz
layer
Ksp + Pl
+ Bi
e
S
N
And + Bi
Ksp + Pl + Q pockets
f

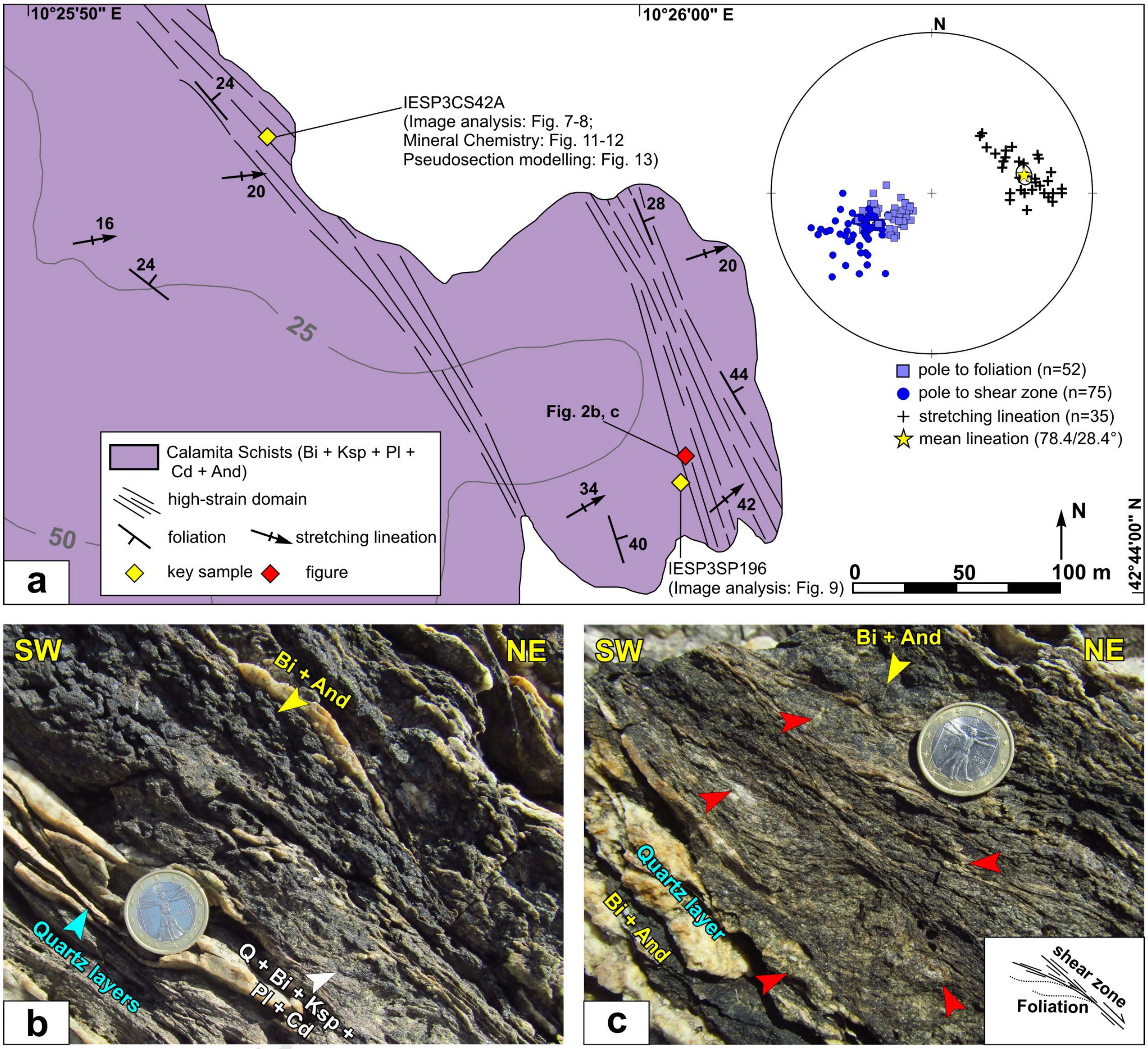
10°25'50" E
10°26'00" E
42°44'00" N
IESP3CS42A
(Image analysis: Fig. 7-8;
Mineral Chemistry: Fig. 11-12
Pseudosection modelling: Fig. 13)
Fig. 2b, c
IESP3SP196
(Image analysis: Fig. 9)
Calamita Schists (Bi + Ksp + Pl + Cd + And)
high-strain domain
foliation
stretching lineation
key sample
figure
pole to foliation (n=52)
pole to shear zone (n=75)
stretching lineation (n=35)
mean lineation (78.4/28.4°)
N
0
50
100 m
a
SW
NE
Bi + And
Quartz layers
Q + Bi + Ksp + Pl + Cd
b
SW
NE
Bi + And
Quartz layer
Bi + And
shear zone
Foliation
c

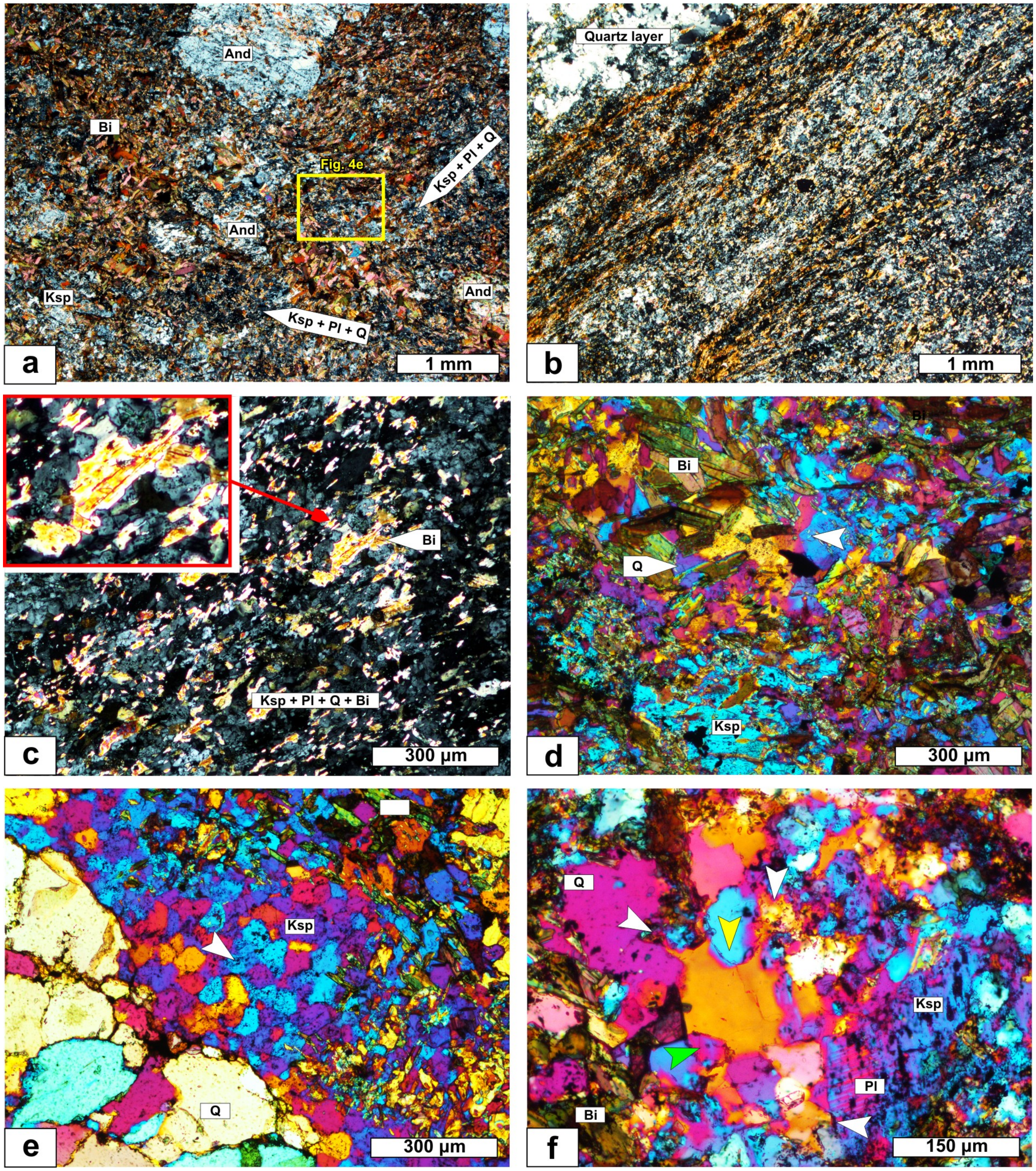
And
Bi
Fig. 4e
Ksp + Pl + Q
And
And
Ksp
Ksp + Pl + Q
a
1 mm
Quartz layer
b
1 mm
Bi
Ksp + Pl + Q + Bi
c
300 µm
Bi
Bi
Q
Ksp
d
300 µm
Ksp
Q
e
300 µm
Q
Ksp
Pl
Bi
f
150 µm

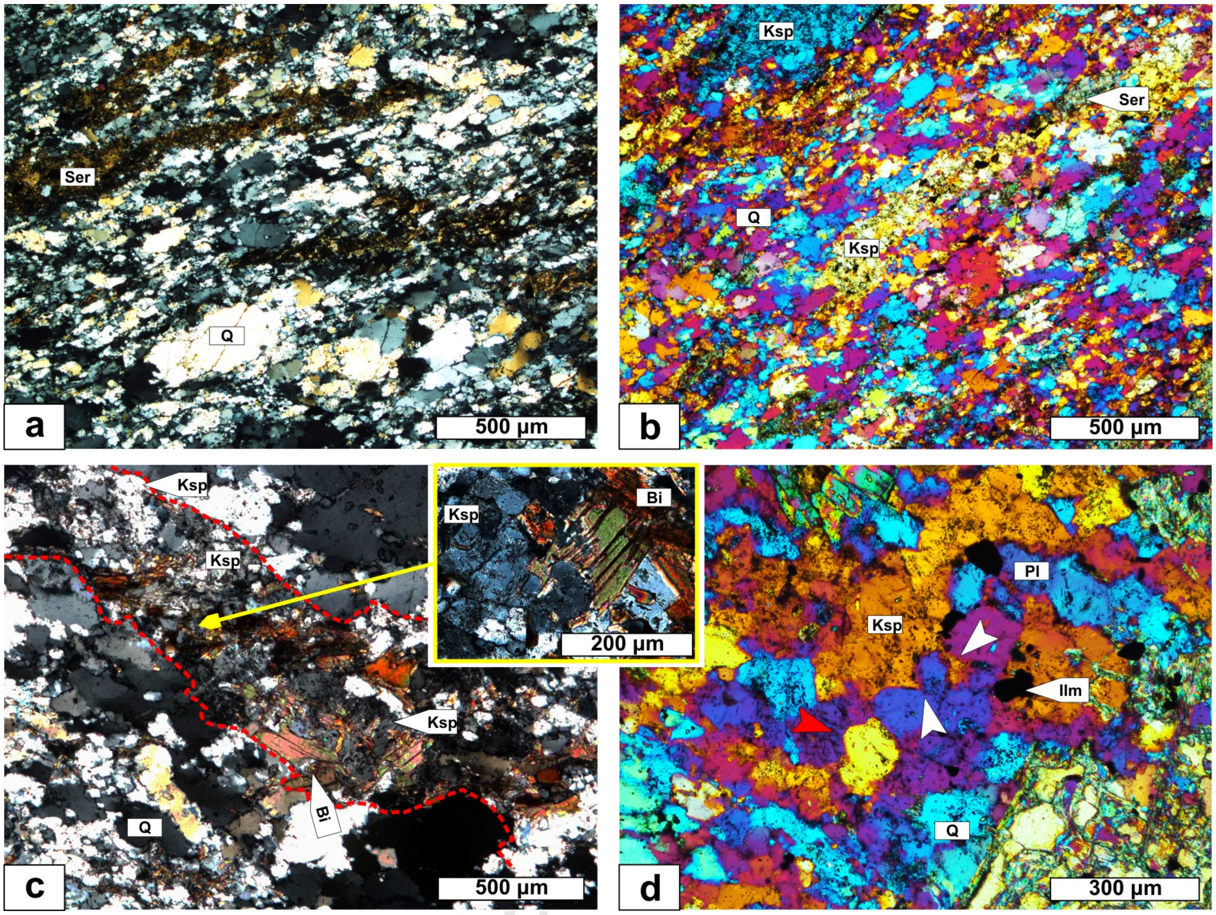
Ser
Q
a
500 µm
Ksp
Ser
Q
Ksp
b
500 µm
Ksp
Ksp
Ksp
Bi
Q
c
500 µm
Ksp
Bi
200 µm
Pl
Ksp
Ilm
Q
d
300 µm

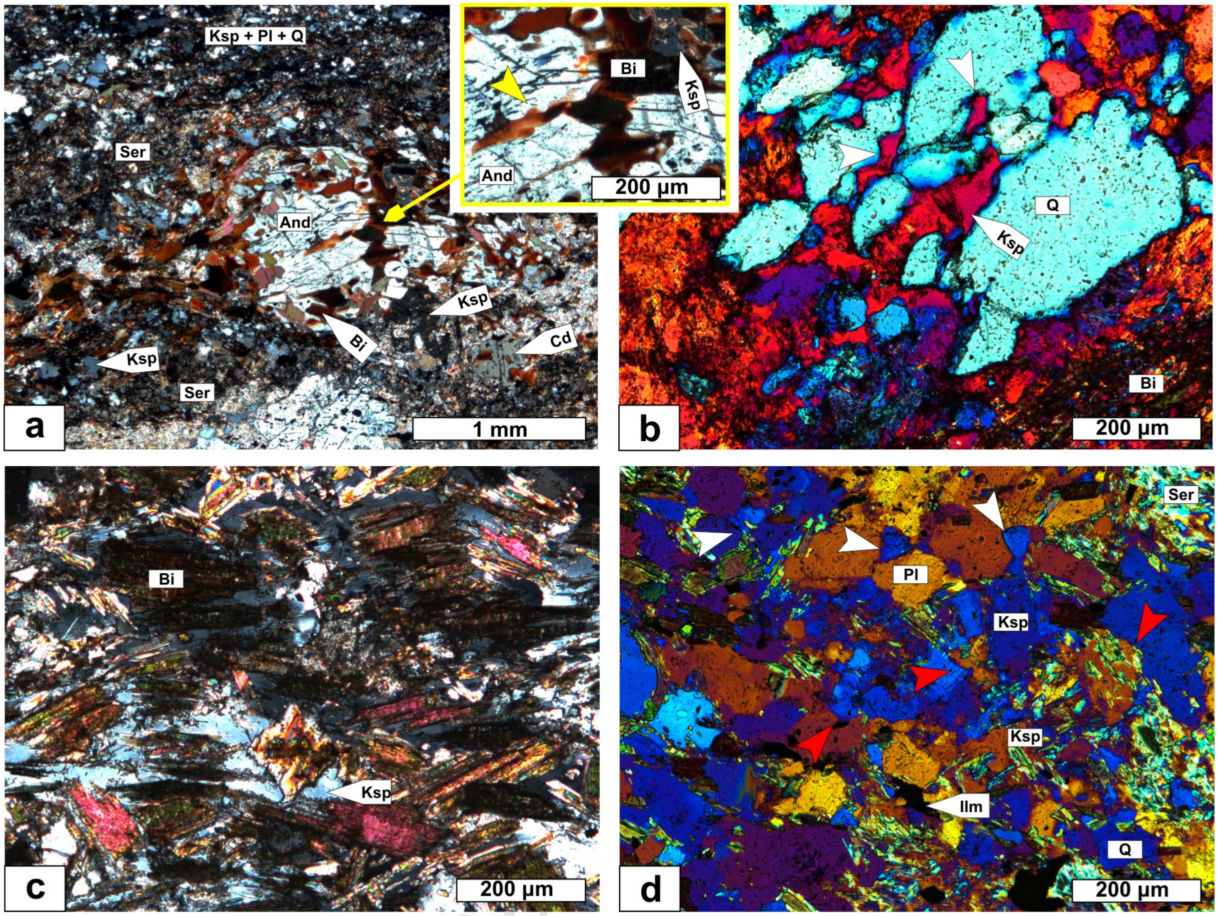
Ksp + Pl + Q
Ser
And
Bi
Ksp
Cd
Ksp
Ser
a
1 mm
Bi
Ksp
And
200 µm
Q
Ksp
Bi
b
200 µm
Bi
Ksp
c
200 µm
Ser
Pl
Ksp
Ksp
Ilm
Q
d
200 µm

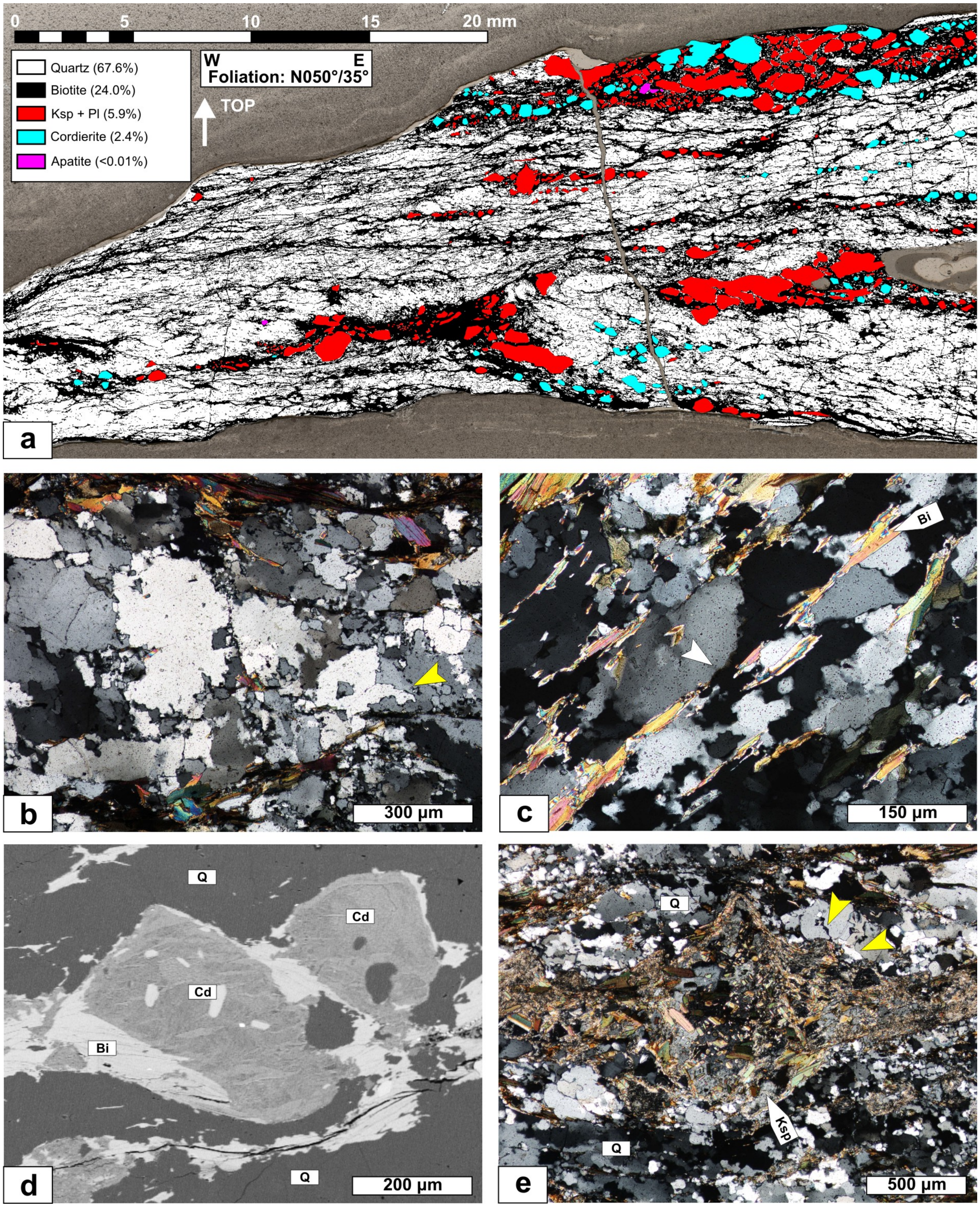

0
5
10
15
20 mm
Quartz (67.6%)
Biotite (24.0%)
Ksp + Pl (5.9%)
Cordierite (2.4%)
Apatite (<0.01%)
W
E
Foliation: N050°/35°
TOP
a
b
300 µm
c
Bi
150 µm
d
Q
Cd
Cd
Bi
Q
200 µm
e
Q
Ksp
Q
500 µm

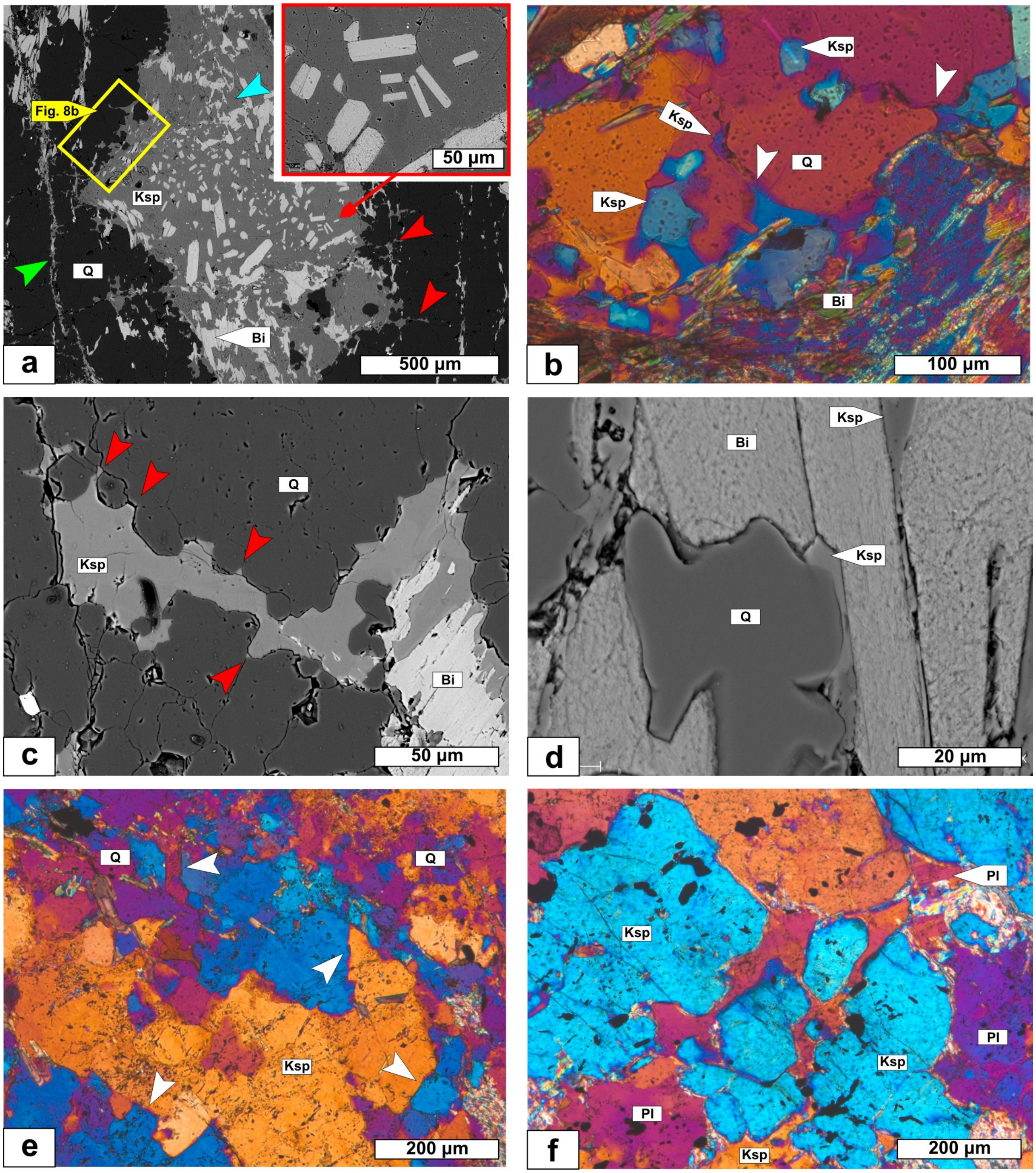
Fig. 8b
Ksp
Q
Bi
50 µm
500 µm
a
Ksp
Ksp
Q
Ksp
Bi
100 µm
b
Q
Ksp
Bi
50 µm
c
Ksp
Bi
Ksp
Q
20 µm
d
Q
Q
Ksp
200 µm
e
Pl
Ksp
Pl
Ksp
Pl
Ksp
200 µm
f

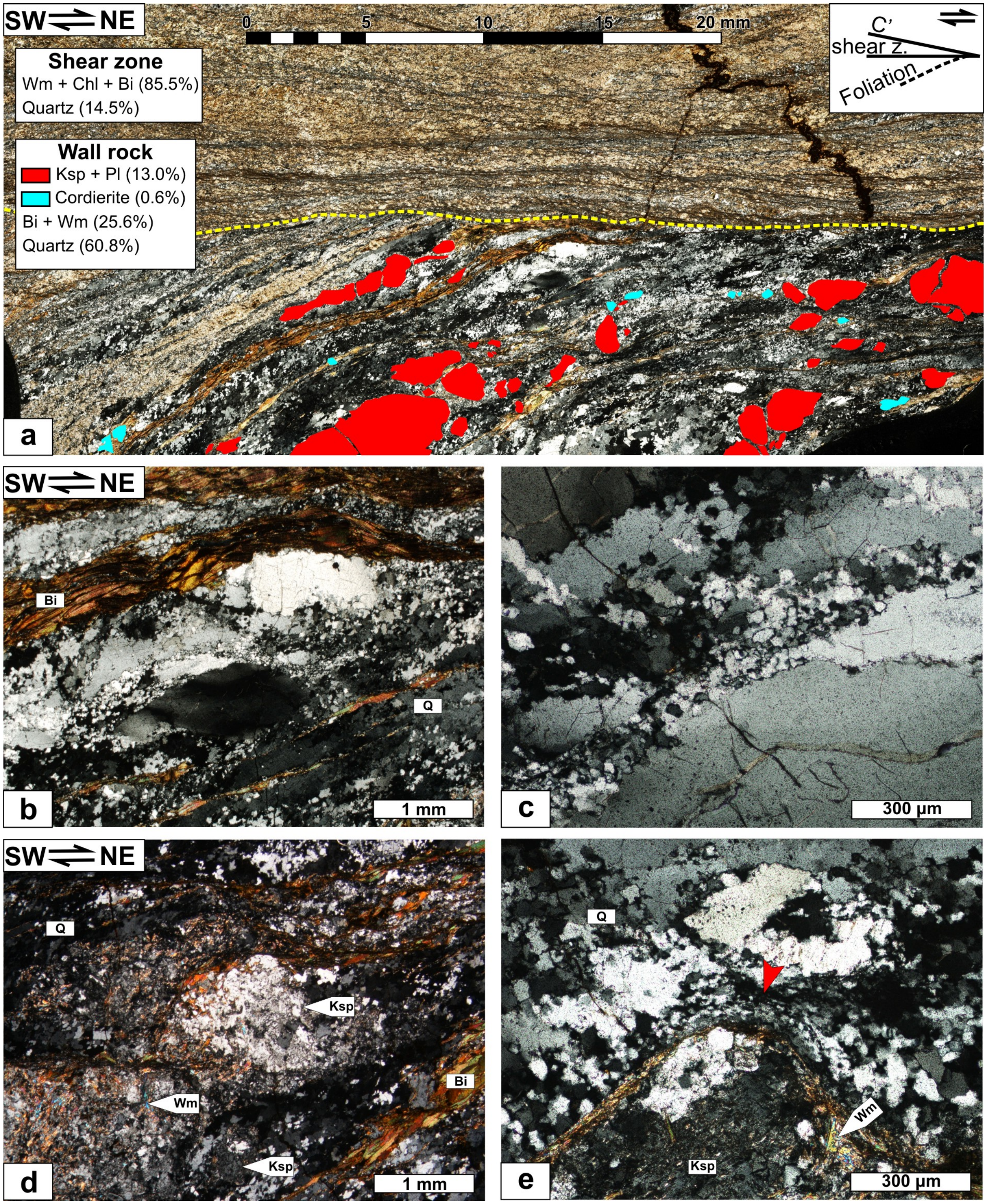

SW NE
0
5
10
15
20 mm
C'
shear z.
Foliation
Shear zone
Wm + Chl + Bi (85.5%)
Quartz (14.5%)
Wall rock
Ksp + Pl (13.0%)
Cordierite (0.6%)
Bi + Wm (25.6%)
Quartz (60.8%)
a
SW NE
Bi
Q
b
1 mm
c
300 µm
SW NE
Q
Ksp
Wm
Bi
Ksp
d
1 mm
Q
Wm
Ksp
e
300 µm

Highlights:

- K-feldspar + plagioclase patches record in-situ partial melting in the upper crust;
- Melting was caused by granite emplacement and occurred in the andalusite field;
- Deformation is distributed in the partially molten rocks;
- Melt crystallization causes strain localization into mylonitic shear zones;